ORIGINAL RESEARCH ARTICLE

# Microstructure and Properties of Chromium Boride–Chromium Carbide–Alumina Composite Coatings Prepared by Reactive Plasma Spraying

Yan-wei Wang[1] · Yong Yang[1] · Han Li[1] · Xian-xing Ren[1] · Wei Tian[2]

**Abstract** A chromium boride–chromium carbide–alumina composite coating was prepared in situ on a Ti-6Al-4V titanium alloy substrate by plasma spraying of $Cr_2O_3$-Al-$B_4C$ composite powder. The results show that, in the process of plasma spraying the $Cr_2O_3$-Al-$B_4C$ composite powder, a chemical reaction occurred among $Cr_2O_3$, Al, and $B_4C$, and $CrB_2$, $Cr_3C_2$, and $\gamma$-$Al_2O_3$ phases with nanosize were formed in situ in the composite coating. Compared with the coating prepared by plasma spraying $CrB_2$-$Cr_3C_2$-$Al_2O_3$ composite powder, the coating prepared by the $Cr_2O_3$-Al-$B_4C$ composite powder has a more uniform and refined microstructure, lower porosity, higher microhardness, better toughness, excellent scratch resistance, and sliding wear resistance. This is attributed to the densification effect and to the fine grain strengthening and toughening effect of nanocrystals produced by the participation of the in situ chemical reactions in the plasma spraying process of the $Cr_2O_3$-Al-$B_4C$ composite powder.

**Keywords** chromium boride–chromium carbide–alumina composite coating · in situ reaction · plasma spraying · scratch resistance · sliding wear resistance

✉ Yong Yang
yangyonghebut@163.com; yangyong@hebut.edu.cn

1  Key Lab. for New Type of Functional Materials in Hebei Province, School of Materials Science and Engineering, State Key Laboratory of Reliability and Intelligence of Electrical Equipment, Tianjin Key Laboratory of Materials Laminating Fabrication and Interface Control Technology, Hebei University of Technology, Xiping Road No. 5340, Beichen District, Tianjin 300401, People's Republic of China

2  AECC Sichuan Gas Turbine Establishment, Chengdu 610500, Sichuan Province, People's Republic of China

## Introduction

Since the 1950s, titanium alloys have been widely used as structural materials in machinery, aviation, shipbuilding, biomedicine, and other fields because of their high specific strength, toughness, and corrosion resistance (Ref 1). However, the application of titanium alloys is limited due to their low hardness and poor wear resistance. (Ref 2). In order to improve the surface hardness and wear resistance of titanium alloys, surface alloying and coating methods have been widely used, including, e.g., laser alloying (Ref 3, 4), nitriding (Ref 5), electroless plating (Ref 6, 7), laser cladding (Ref 8-10), magnetron sputtering (Ref 11), micro-arc oxidation (Ref 12, 13), etc. Although the above processes improve the surface hardness and wear resistance of the titanium alloy matrix to a certain extent, they also have the disadvantages of expensive equipment, long process cycle, and thin films. In addition to the above processes, the thermal spraying process is also the most widely used surface modification process. Among the thermal spraying processes, plasma spraying is often used in the surface modification of titanium alloys due to its advantages of simple operation, wide range of sprayable materials, high coating thickness, and controllability (Ref 14).

Some oxide and carbide ceramic systems have received more attention in the preparation of wear-resistant coating materials by plasma spraying, including $Al_2O_3$-$TiO_2$ (Ref 15-17) and a hard cermet system, such as WC-Co (Ref 18), TiC-Co (Ref 19), and $Cr_3C_2$-NiCr (Ref 20, 21). However, with the change of service environment, the requirements for wear resistance of titanium alloys are getting higher and higher, but the improvement of wear resistance of the above coating material system is limited. Among the transition metal borides and carbides, $CrB_2$ and $Cr_3C_2$ have the characteristics of high melting point, high hardness,

excellent wear resistance, corrosion resistance, and high-temperature oxidation resistance, so they can be used as candidate materials for surface modification of titanium alloys (Ref 22, 23). For example, when 15 wt% $CrB_2$ was added to a NiAl coating, the wear rate decreased by about 70 % compared with that of the pure NiAl coating (Ref 24). In previous studies, a $CrB_2$-$Cr_3C_2$ binary composite ceramic coating has been prepared on a Ti-6Al-4V alloy substrate by plasma spraying, showing high hardness and wear resistance, but the porosity of the coating was high, and the mechanical properties of the coating needed to be further improved (Ref 25).

Thermite reaction is the reaction between thermite and metal oxide. The heat released by the reaction is high, and it has been widely used in the process of material preparation (Ref 26, 27). Some researchers have prepared composites with two main phases of chromium boride, chromium carbide, and alumina by reactive synthesis. For example, Yeh et al. (Ref 28) used $Cr_2O_3$, Al, and B powders as raw materials to obtain chromium boride–alumina composites by introducing a thermite reaction in the process of self-propagating combustion, indicating that $B_4C$ as the boron source can reduce the loss of B in the reaction process. Yeh et al. (Ref 29) prepared $Cr_3C_2$-$Al_2O_3$ composites by self-propagating high-temperature synthesis with $Cr_2O_3$, Al, and carbon black as raw materials, and found that the $Cr_7C_3$ second phase existed in the material due to a small amount of C loss. In addition, studies have shown that the introduction of $Al_2O_3$ can improve the strength and toughness of ceramic materials (Ref 30-32). In this work, we considered introducing a thermite reaction into the preparation of a $CrB_2$-$Cr_3C_2$ composite ceramic coating, and introducing an $Al_2O_3$ phase in situ to improve the compactness and mechanical properties of the coating.

In this study, $Cr_2O_3$, Al, and $B_4C$ were used as raw materials. $Cr_2O_3$-Al-$B_4C$ composite powder was prepared by the spray drying method. Then, the chromium boride–chromium carbide–alumina composite ceramic coating was prepared on the Ti-6Al-4V alloy substrate by plasma spraying $Cr_2O_3$-Al-$B_4C$ composite powder. The phase composition, microstructure, microhardness, toughness, scratch resistance, and sliding wear resistance properties of the coating and the reaction mechanism of the $Cr_2O_3$-Al-$B_4C$ composite powder have been investigated. Meanwhile, a chromium boride–chromium carbide–alumina composite ceramic coating was prepared by plasma spraying $CrB_2$-$Cr_3C_2$-$Al_2O_3$ composite powder. The microstructure and properties of the two chromium boride composite coatings have been compared and analyzed.

## Materials and Methods

### Preparation of Composite Coatings

Commercial $CrB_2$ (1–5 μm, 99.5% purity), $Cr_3C_2$ (5–8 μm, 99.0% purity), $Al_2O_3$ (40 nm, 99.0% purity), $Cr_2O_3$ (1–5 μm, 99.9% purity), Al (6–9 μm 99.8% purity), and $B_4C$ (1–5 μm, 99.9% purity) powders were used as raw materials (see Fig. 1). The milled raw powders, deionized water, polymeric binder, and dispersant were mixed to form slurries, and then two composite powders of $CrB_2$-$Cr_3C_2$-$Al_2O_3$ and $Cr_2O_3$-Al-$B_4C$ were obtained by spray drying. The inlet and outlet temperatures of the spray drying were 250 and 120 °C, respectively. The mass ratio was 35.5:21.6:42.9 for $CrB_2/Cr_3C_2/Al_2O_3$, and 63.9:13.4:22.7 for $Cr_2O_3/Al/B_4C$. There were two sizes of the substrate material (Ti-6Al-4V titanium alloy, with high specific strength and comprehensive mechanical properties). One was $\Phi$20 mm × 10 mm for the wear samples, the other was 10 mm × 10 mm × 12 mm for the other samples. Before spraying, the surface of the substrate was sandblasted and degreased to increase the surface roughness $R_a$ to around 6–8 μm). Then, a bond coating of Ni–20wt%Al alloy was deposited on the pretreated substrate surface. Finally, the $CrB_2$-$Cr_3C_2$-$Al_2O_3$ and $Cr_2O_3$-Al-$B_4C$ composite powders were deposited on the bond coating as the top coating. The GP-80-type air plasma spraying equipment (China Jiujiang) was employed to produce the bond coating and top coating with thicknesses of 250 μm. The parameters of plasma spraying were: current 500 A; voltage: 70 V; primary gas (Ar) flow 150 dm³/min; secondary gas ($H_2$) flow 30 dm³/min; spraying distance: 100 mm; powder feeding rate 20–30 g/min; and moving speed of spray gun 200 mm/s. After deposition, the as-sprayed samples were polished using 600-, 1000-, and 1500-grit SiC papers.

### Scratch and Wear Test

The scratch resistance of the composite coatings was measured by a WS-2005 automatic scratch tester with an acoustic emission signal detection system (Lanzhou Zhongke Kaihua Technology Development). The scratches were linear and the normal load was progressively increased. The parameters were: indenter was loaded up to 60 N at the rate of 30 N/min, scratch speed was 1 mm/min, and scratch length was 2 mm. Dry sliding wear tests of the composite coatings were carried out by a SFT-2 M ball-on-disc friction and wear tester (Lanzhou Zhongke Kaihua Technology Development). Commercial bearing grade $Si_3N_4$ balls with a diameter of 4 mm were used as the counter surface specimen. The parameters were set as: the

**Fig. 1** SEM micrographs of the raw powders: (a) Al; (b) Al$_2$O$_3$; (c) Cr$_2$O$_3$; (d) CrB$_2$; (e) B$_4$C; (f) Cr$_3$C$_2$
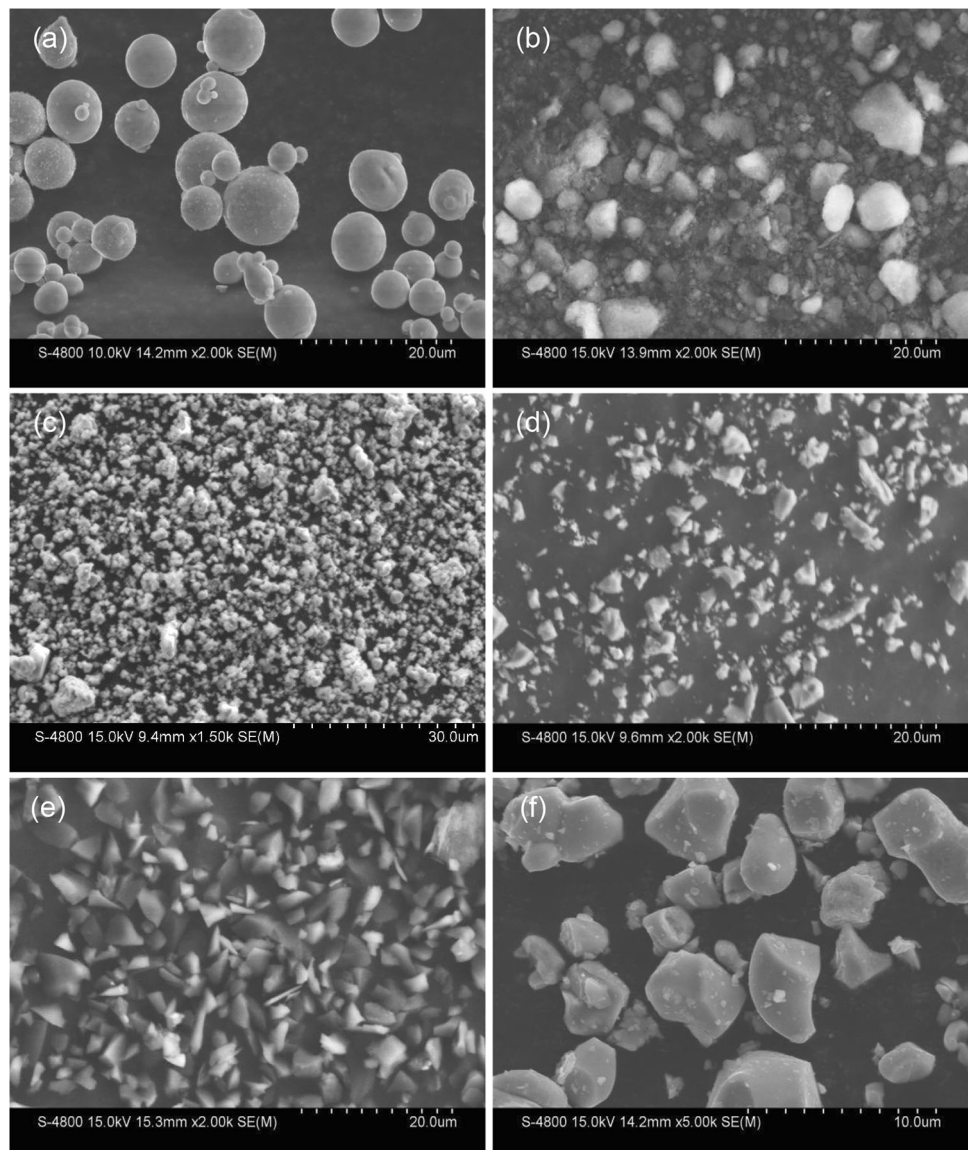


load was 30 N, the load time was 10 min, track radius was 3 mm, and the speed was 400 rpm. The measurement method was cyclic friction, and wear experiments were conducted on the polished coating surface (roughness $R_a$ was about 1 μm). The wear rate was calculated according to following Eq 1:

$$W = \frac{V}{2\pi rntN} \qquad \text{(Eq 1)}$$

where $V$ is the wear volume (mm$^3$), $r$ is the track radius (m), $n$ is the speed (rpm), $t$ is the running time (min), and $N$ is the load (N). The number of repeated wear tests was three.

## Sample Characterization

An x-ray diffractometer (DMAX-2500; Rigaku) with Cu Kα radiation was used to identify the phase composition of the raw powders, composite powders, and coatings. Based on the SEM images of the powders, the particle size distribution of the powders was obtained by image analysis. The scanning mode of the diffractometer was continuous, the power was 6 kW, the scanning angle ranged from 10 to 80°, and the scanning rate of the powder and coating was 4°/min. A scanning electron microscope (FE-SEM; S-4800; Hitachi) equipped with the EDAX-AMETEK

energy spectrometer (EDS) was used for microstructure analyses of the powders and the coatings. The microstructure of the coating obtained by plasma spraying of the $Cr_2O_3$-Al-$B_4C$ composite powder was characterized by transmission electron microscopy (TEM; Tec-nai F20; Philips). The thermal property of $Cr_2O_3$-Al-$B_4C$ composite powder was tested using a thermal analyzer (TG/DTA 6300; Seiko) in Ar gas at a heating rate of 10 °C/min up to 1300 °C. The porosity of the coatings were analyzed by 20 scanning images of polished cross-sections using image analysis. These images were taken at ×500 magnification. The microhardness of the coatings was measured using a microhardness tester (HMV-2; SHIMADZU). The indenter was a Vickers pyramid diamond, the load was 0.1 kgf, and the dwell time was 15 s. To reduce the error, 20 measurements were carried out to give an averaged hardness value. The indentation test was performed with a load of 0.3 kgf and a loading time of 15 s. The toughness of the coatings was analyzed by observing the indentation and fracture morphology under SEM.

## Results and Discussion

### Microstructure of the $CrB_2$-$Cr_3C_2$-$Al_2O_3$ and $Cr_2O_3$-Al-$B_4C$ Composite Powder

Figure 2(a) and (b) shows the XRD patterns of the $CrB_2$-$Cr_3C_2$-$Al_2O_3$ and $Cr_2O_3$-Al-$B_4C$ composite powders, respectively. It can be seen that the $CrB_2$-$Cr_3C_2$-$Al_2O_3$ composite powder consists of $CrB_2$, $Cr_3C_2$ and α-$Al_2O_3$, and that the $Cr_2O_3$-Al-$B_4C$ composite powder consists of $Cr_2O_3$, Al and $B_4C$, which indicates that the phases of the composite powders were consistent with that of the raw powders after spray drying. The SEM micrographs of the $CrB_2$-$Cr_3C_2$-$Al_2O_3$ and $Cr_2O_3$-Al-$B_4C$ composite powders are shown in Fig. 3(a) and (b), respectively, and the

spherical or nearly spherical morphology in these two composite powders can be seen. Figure 3(c) and (d) shows the EDS results of region A and region B, respectively, indicating that the two composite powders contain Cr, B, C, O and Al, which is consistent with the XRD results. The particle size distribution of the $CrB_2$-$Cr_3C_2$-$Al_2O_3$ and $Cr_2O_3$-Al-$B_4C$ composite powders are shown in Fig. 3(e) and (f), respectively, and their $D_{50}$ values are 31 μm and 32 μm, respectively. Table 1 shows the parameters characterizing the fluidity of the two composite powders. The closer the ratio of the tap density to the apparent density is to 1, the better the fluidity. According to the literature (Ref 33), the spray-dried powder (apparent density $> 1.7 \times 10^3$ kg/m$^3$, $D_{50} > 20$ μm) can be directly used to prepare plasma-sprayed coatings without further densification. Therefore, the $CrB_2$-$Cr_3C_2$-$Al_2O_3$ and $Cr_2O_3$-Al-$B_4C$ composite powders used in this experiment meet the requirements of plasma spraying.

### Microstructure of the Two Chromium Boride–Chromium Carbide–Alumina Composite Coatings

The coating prepared by plasma spraying the $CrB_2$-$Cr_3C_2$-$Al_2O_3$ composite powder consists of $CrB_2$, CrB, $Cr_3C_2$, α-$Al_2O_3$, γ-$Al_2O_3$ and a small amount of $Cr_2O_3$, as shown in Fig. 4(a). The XRD result indicated that many $CrB_2$, $Cr_3C_2$ and α-$Al_2O_3$ were retained in the coating after plasma spraying, and, in addition, new phases CrB, γ-$Al_2O_3$ and $Cr_2O_3$ were also formed in the coating. A small amount of oxygen in the environment may be drawn into the plasma jet during plasma spraying, resulting in the oxidation of the raw powders. The formation of CrB may be caused by Eq. 2. $B_2O_3$ was not detected in Fig. 4(a), the possible reason being that $B_2O_3$ volatilized as a gas (Ref 34) or remained in the coating as an amorphous phase (Ref 35). The formation of $Cr_2O_3$ may be related to Eq. 2–5:
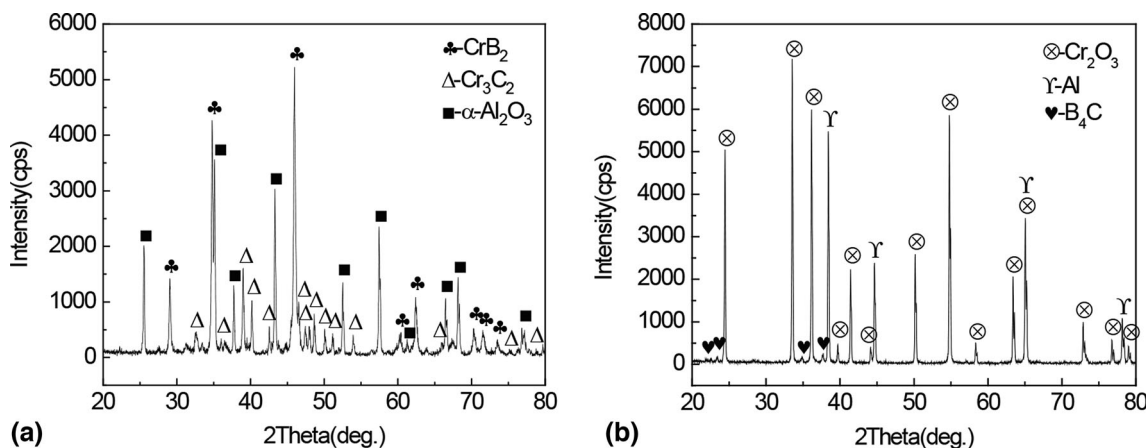


**Fig. 2** XRD patterns of the composite powders: (a) $CrB_2$-$Cr_3C_2$-$Al_2O_3$, and (b) $Cr_2O_3$-$B_4C$-Al

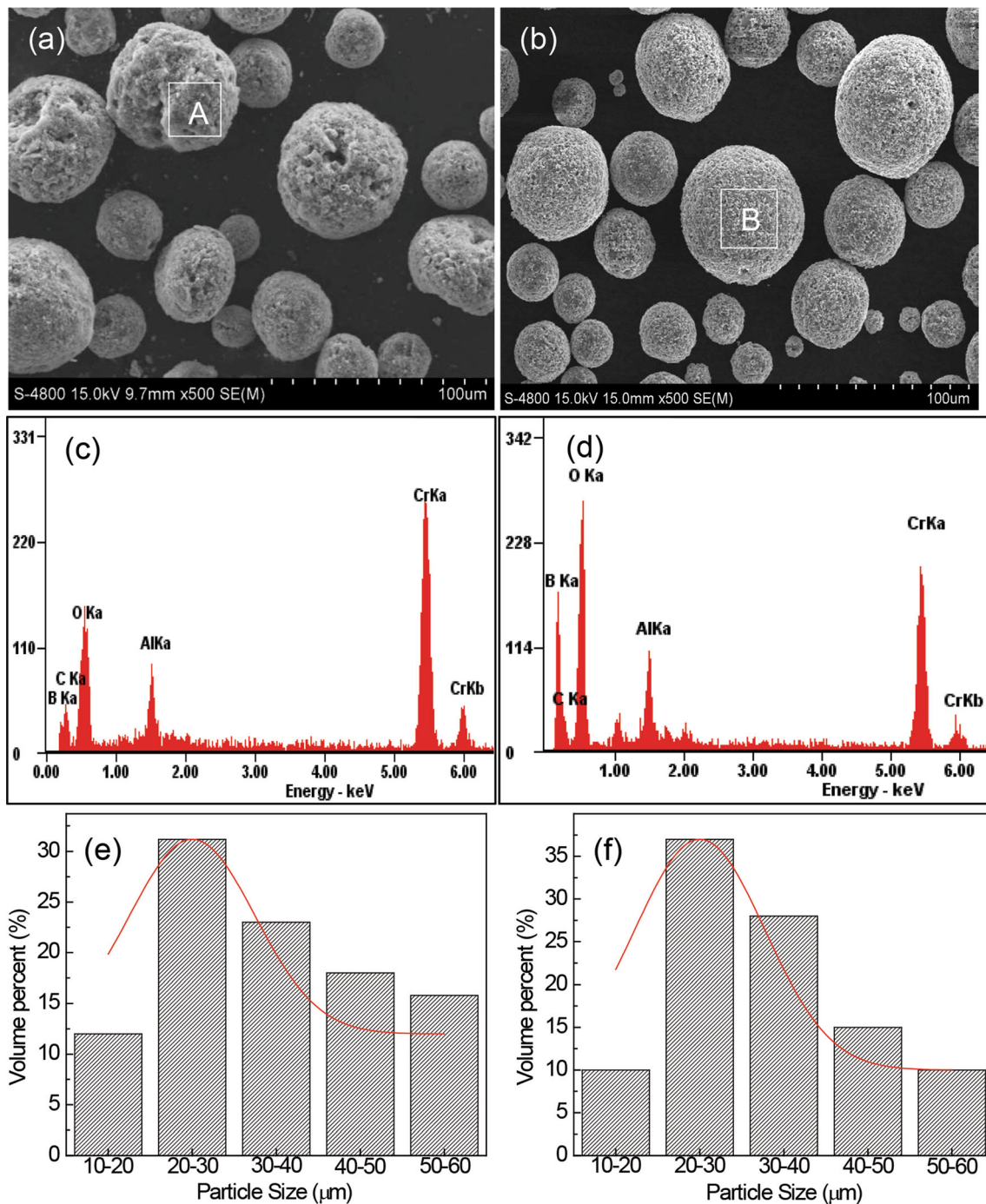**Fig. 3** SEM micrographs, EDS, and particle size distribution results of the composite powders: (a), (c), (e) $CrB_2$-$Cr_3C_2$-$Al_2O_3$, and (b), (d), (f) $Cr_2O_3$-Al-$B_4C$

**Table 1** Properties of the two composite powders

| System | Apparent density, g/ml | Tap density, g/ml | Tap density/apparent density | Flowability, s/50 g |
|---|---|---|---|---|
| $CrB_2$-$Cr_3C_2$-$Al_2O_3$ | 1.951 | 2.185 | 1.120 | 5.28 |
| $Cr_2O_3$-Al-$B_4C$ | 1.864 | 2.274 | 1.220 | 5.45 |
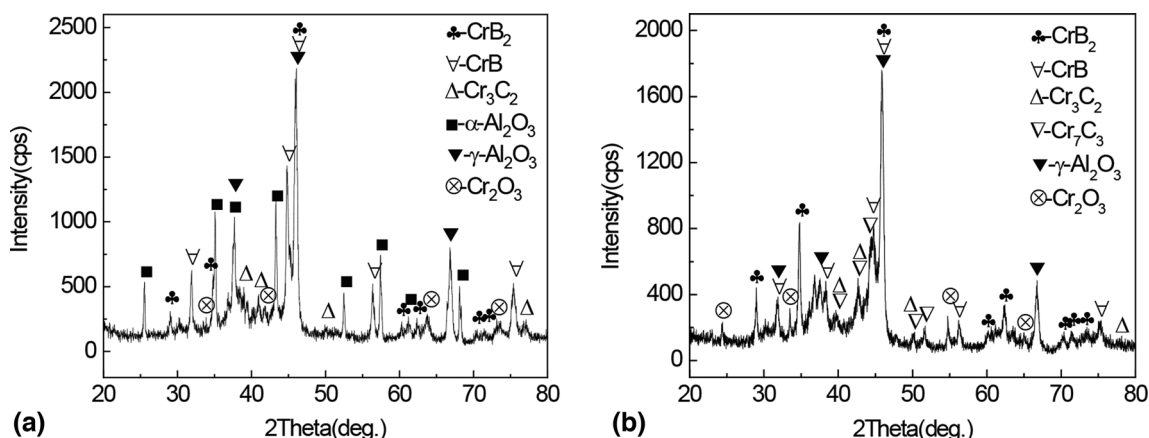
**Fig. 4** XRD patterns of the composite coatings: (a) $CrB_2$-$Cr_3C_2$-$Al_2O_3$, and (b) $Cr_2O_3$-$B_4C$-Al

$$12CrB_2 + 21O_2 \rightarrow 4CrB + 4Cr_2O_3 + 10B_2O_3 \quad \text{(Eq 2)}$$

$$4CrB_2 + 9O_2 \rightarrow 2Cr_2O_3 + 4B_2O_3 \quad \text{(Eq 3)}$$

$$4Cr_3C_2 + 17O_2 \rightarrow 6Cr_2O_3 + 8CO_2 \quad \text{(Eq 4)}$$

$$4Cr_3C_2 + 13O_2 \rightarrow 6Cr_2O_3 + 8CO \quad \text{(Eq 5)}$$
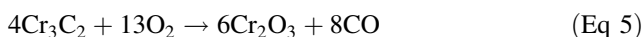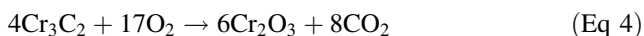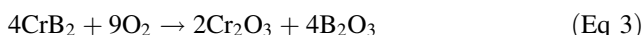
It has been reported that the phase transformation from $\alpha$-$Al_2O_3$ to $\gamma$-$Al_2O_3$ can be attributed to the small critical nucleation free energy of $\gamma$-$Al_2O_3$ (Ref 36), thus molten $Al_2O_3$ was more likely to nucleate preferentially $\gamma$-$Al_2O_3$ instead of $\alpha$-$Al_2O_3$ under plasma spraying conditions (metastable conditions of rapid cooling and solidification). Figure 4(b) shows the XRD pattern of the coating prepared by plasma spraying the $Cr_2O_3$-Al-$B_4C$ composite powder. It can be seen from the figure that the coating consists of CrB, CrB, $Cr_3C_2$, $Cr_7C_3$, $\gamma$-$Al_2O_3$ and a small amount of $Cr_2O_3$. Compared with Fig. 2(b), it can be seen that a chemical reaction occurred between $Cr_2O_3$, $B_4C$ and Al in the $Cr_2O_3$-Al-$B_4C$ composite powder during spraying. The specific reaction process is analyzed in detail in Section 3.3.

Figure 5(a) and (c) shows the cross-sectional SEM micrographs of the coatings prepared by plasma spraying the $CrB_2$-$Cr_3C_2$-$Al_2O_3$ and $Cr_2O_3$-Al-$B_4C$ composite powders, respectively. As shown in Fig. 5(a) and (c), there are large pores in the coating prepared by plasma spraying the $CrB_2$-$Cr_3C_2$-$Al_2O_3$ composite powder, compared with the coating prepared by plasma spraying the $CrB_2$-$Cr_3C_2$-$Al_2O_3$ composite powder, with the microstructure of the coating prepared by plasma spraying the $Cr_2O_3$-Al-$B_4C$ composite powder being more compact, showing only a few small spherical pores. The porosity of the coatings prepared by plasma spraying the $CrB_2$-$Cr_3C_2$-$Al_2O_3$ and $Cr_2O_3$-Al-$B_4C$ composite powders are $8.7 \pm 1.2$ and $5.4 \pm 0.7\%$, respectively, which also indicate that the latter had better compactness. Figure 5(b) is a partial enlarged view of Fig. 5(a), and the EDS results of the gray area A

and the black area B are shown in Table 2. The results show that region A contained Cr, B and C elements. Combined with the XRD results, it is speculated that region A may be enriched in $CrB_2$, CrB, and $Cr_3C_2$. Region B contains Al and O elements, and, combined with the XRD results, it is speculated that this region may be enriched in the $Al_2O_3$ phase. It can be seen from Fig. 5(b) that the microstructure of the coating presents a certain lamellar distribution, but it can also be seen that the gray structure is mostly distributed in blocks, showing a poor melting state. Compared with the borides and carbides of other transition metals (Ti and Zr), the borides and carbides of Cr have relatively low melting points, but higher specific heat capacity. The larger the specific heat capacity, the worse the thermal conductivity, and the powders are difficult to melt. In addition, although the temperature of the plasma jet is high (the temperature at the flame center can be as high as 10,000–15,000 K), the flame velocity is about 200 m/s, so the residence time of powder particles in the flame flow is very short ($10^{-4}$ to $10^{-3}$ s), resulting in the insufficient melting (Ref 37, 38). The black structure was distributed in thin bands and filled in the gaps of the gray block structure, which improved the compactness of the coating to a certain extent, indicating that the melting degree of the nano-$Al_2O_3$ in the plasma jet was better. Although the melting point of $Al_2O_3$ is also high (2040 °C), compared with $CrB_2$ and $Cr_3C_2$, the specific surface area of the nano-$Al_2O_3$ is larger, so the heating area of the powders is increased, which results in the improved melting degree. Figure 5(d) is a partial enlarged image of Fig. 5(c), form which it can be seen that the phases in the coating prepared by plasma spraying the $Cr_2O_3$-Al-$B_4C$ composite powder were distributed in lamellae, the microstructure distribution was more uniform and there were fewer microdefects. Figure 5(e) is a high-magnification micrograph of the coating prepared by plasma spraying the $Cr_2O_3$-Al-$B_4C$ composite powder. The EDS results

**Fig. 5** SEM micrographs of the cross-section of the coatings obtained by plasma spraying (a), (b) $CrB_2$-$Cr_3C_2$-$Al_2O_3$, and (c), (d), (e) $Cr_2O_3$-Al-$B_4C$
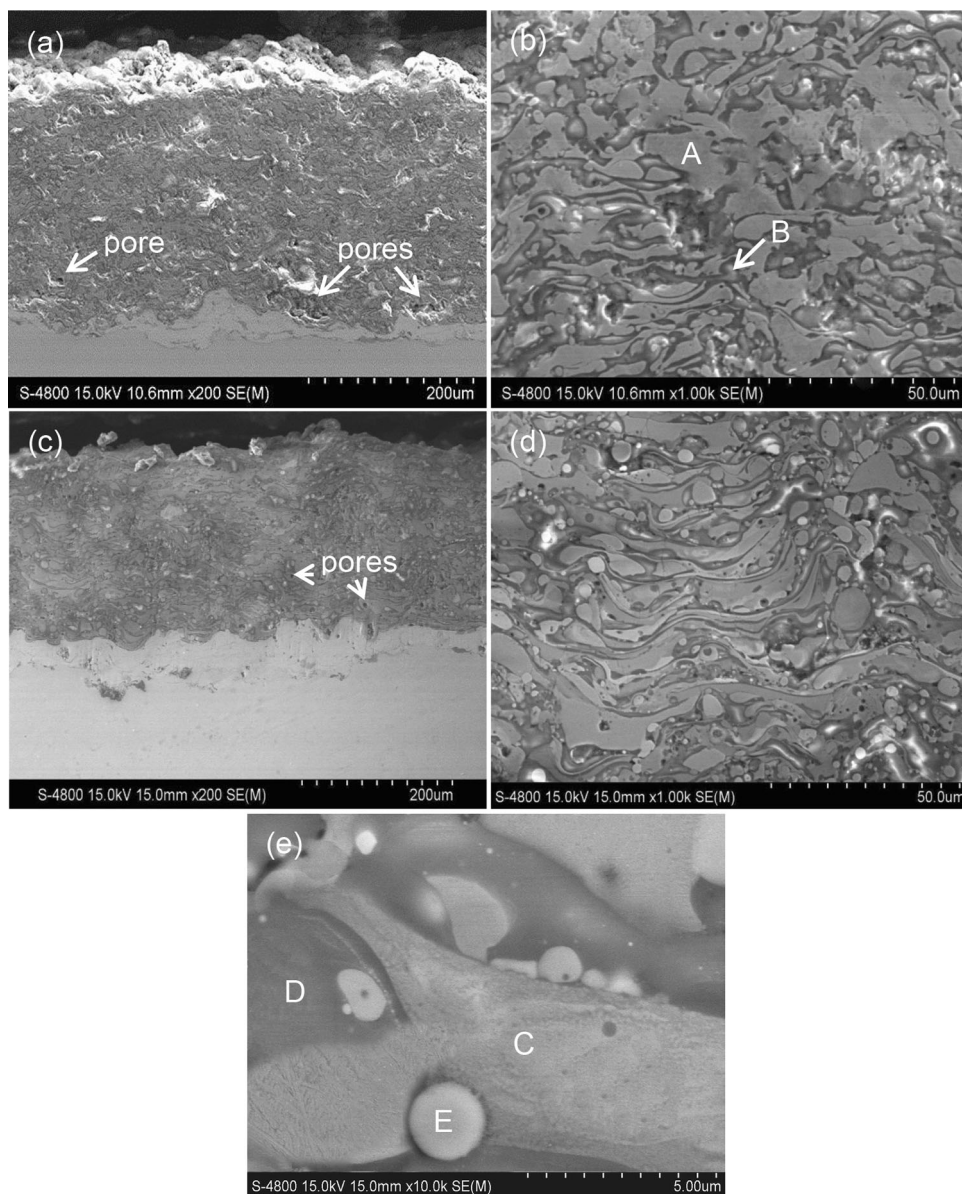


**Table 2** EDS results of the two composite coatings

| Element, wt%) | Cr | B | C | Al | O |
|---|---|---|---|---|---|
| A | 56.40 | 32.49 | 11.12 | … | … |
| B | 6.21 | 3.06 | 4.03 | 49.42 | 37.28 |
| C | 61.38 | 15.64 | 22.98 | … | … |
| D | … | … | … | 52.94 | 47.06 |
| E | 68.42 | … | … | … | 31.58 |

of areas C, D, and E in Fig. 5(e) are shown in Table 3. Combined with the XRD results, it is speculated that the dark gray area C is rich in $CrB_2$ and $Cr_3C_2$, and that the black area D is rich in $\gamma$-$Al_2O_3$, and that the spherical

particles (region E) are unreacted $Cr_2O_3$. It can be seen that region C is composed of particles with a fine and uniform structure. The phase interface of region C and region D is relatively pure, which may be due to the in situ reaction of the composite powder, so as to avoid the pollution of the powder particle surface such as oxidation in the traditional spraying process, reduce defects, and improve the compactness of the coating.

Figure 6 shows TEM images of the coating prepared by plasma spraying the $Cr_2O_3$-Al-$B_4C$ composite powder. Figure 6(a) shows that the grain size range of the equiaxed grains is 50–100 nm, which can be speculated as $CrB_2$ nanograins. Figure 6(b) shows that the grain size of the equiaxed grains is about 100 nm, and the diffraction pattern shows the CrB nanograins. The size of short rod-like

Table 3 Comparison of properties of composite coatings containing chromium boride and chromium carbide.

| Coating composition | Technology | Hardness | Model and counterparts | Wear condition | Coefficient of friction | Wear rate | Ref. |
|---|---|---|---|---|---|---|---|
| NiAl-CrB$_2$ | APS | ... | Pin-on-disc, stainless steel | 150 N, 1.4 m/s, 500 °C | 0.35 | $2.6 \times 10^{-5}$ mm$^3$/N m | Ref [24] |
| NiCr-Cr$_3$C$_2$ | Atmospheric plasma spray (APS) | $1016 \pm 60$ HV$_{0.3}$ | Ball-on-disk, Si$_3$N$_4$(hardness 91 HRC) | 2 N, 0.2 m/s | 0.65 | $0.98 \times 10^{-4}$ mm$^3$/N m | Ref [50] |
| NiCr-Cr$_3$C$_2$ | Supersonic plasma spray | 962 HV$_{0.3}$ | Pin-on-disk, ZrO$_2$ | 40 N | 0.47 | | Ref [51] |
| Cr$_7$C$_3$,Al$_2$O$_3$ & Ni-Mo-Al alloy | APS | $\sim 600$ HV | Pin-on-disk, cast iron | 20 N, 0.12 m/s | 0.53 | $0.73 \times 10^{-4}$ mm$^3$/N m | Ref [52] |
| $\gamma$-Ni, CrB & Cr$_7$C$_3$ | APS | 570.9 HV$_{0.1}$ | Pin-on-disk, silica sand | 55 N | | $\sim 1 \times 10^3$ mm$^3$/mm | Ref [53] |
| Cr$_7$C$_3$, Cr$_{23}$C$_6$ & Cr$_2$AlC | APS | 857 HV | ... | ... | ... | ... | Ref [54] |
| $\gamma$-Ni, CrB, Cr$_7$C$_3$, TiC et al. | plasma spray welding | 1142 HV$_{0.5}$ | Wheel grinder, SiC abrasive paper | 17 N | | 6 mm$^3$ | Ref [55] |
| CrB$_2$-Cr$_3$C$_2$-Al$_2$O$_3$ | APS | $1230 \pm 115$ HV$_{0.1}$ | Ball-on-disc, Si$_3$N$_4$(hardness 16 GPa) | 30 N, 0.13 m/s | 0.445 | $0.72 \times 10^{-3}$ mm$^3$/N m | This work |

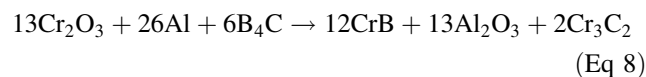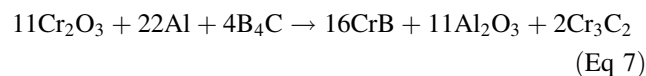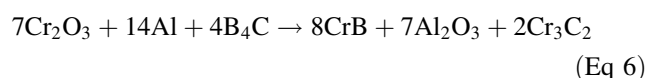**Fig. 6** TEM micrographs of the coating prepared by the $Cr_2O_3$-Al-$B_4C$ composite powder: (a) equiaxed $CrB_2$ nano grains, (b) equiaxed CrB nano grains, (c) short rod-like $\gamma$-$Al_2O_3$ nano grains, (d) nanograins dispersed in the coating
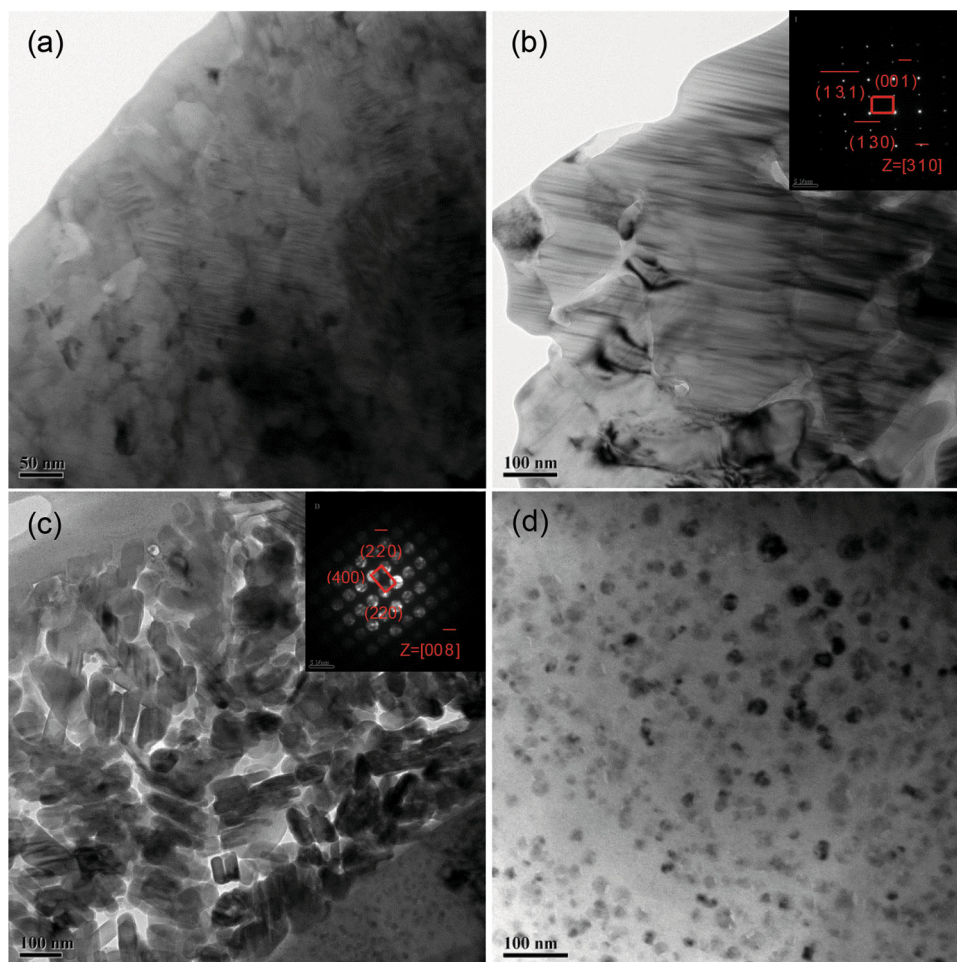
grains shown in Fig. 6(c) is about 100 nm, and the diffraction pattern is calibrated as nano-$\gamma$-$Al_2O_3$. Figure 6(d) shows that equiaxed nanograins with size less than 50 nm are also dispersed in the coating. The above results show that the microstructure of the coating prepared by plasma spraying the $Cr_2O_3$-Al-$B_4C$ composite powder contains many nanophases, and that the microstructure is obviously refined, which can play a key role in strengthening and toughening.

## Reaction Mechanism of the $Cr_2O_3$-Al-$B_4C$ Composite Powder in the Plasma Spraying Process

By comparing the phase analysis results of the $Cr_2O_3$-Al-$B_4C$ composite powder and the composite coating, it can be seen that the $Cr_2O_3$-Al-$B_4C$ system composite powder had an obvious chemical reaction in the process of plasma spraying, and it is speculated that the $Cr_2O_3$, Al, and $B_4C$ raw powders may react during the plasma spraying process as:

$$7Cr_2O_3 + 14Al + 4B_4C \rightarrow 8CrB + 7Al_2O_3 + 2Cr_3C_2 \tag{Eq 6}$$

$$11Cr_2O_3 + 22Al + 4B_4C \rightarrow 16CrB + 11Al_2O_3 + 2Cr_3C_2 \tag{Eq 7}$$

$$13Cr_2O_3 + 26Al + 6B_4C \rightarrow 12CrB + 13Al_2O_3 + 2Cr_3C_2 \tag{Eq 8}$$

$$19Cr_2O_3 + 38Al + 6B_4C \rightarrow 24CrB + 19Al_2O_3 + 2Cr_3C_2 \tag{Eq 9}$$
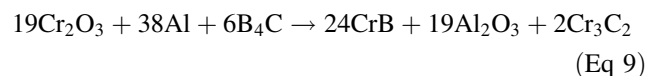
The above reactions were thermodynamically analyzed according to the thermodynamic data manual (Ref 39, 40). The change trend of the Gibbs free energy of Eq. 6–9 with temperature is shown in Fig. 7(a). It can be seen that the Gibbs free energy of the four reactions is less than 0, indicating that the reaction can proceed spontaneously within a given temperature range. The molar enthalpy changes of Eq. 6–9 are shown in Fig. 8, indicating that the four reactions are exothermic. According to the research of Merzhanov et al. (Ref 41), the adiabatic temperature ($T_{ad}$) of the reaction is not less than 1800 K, indicating that a
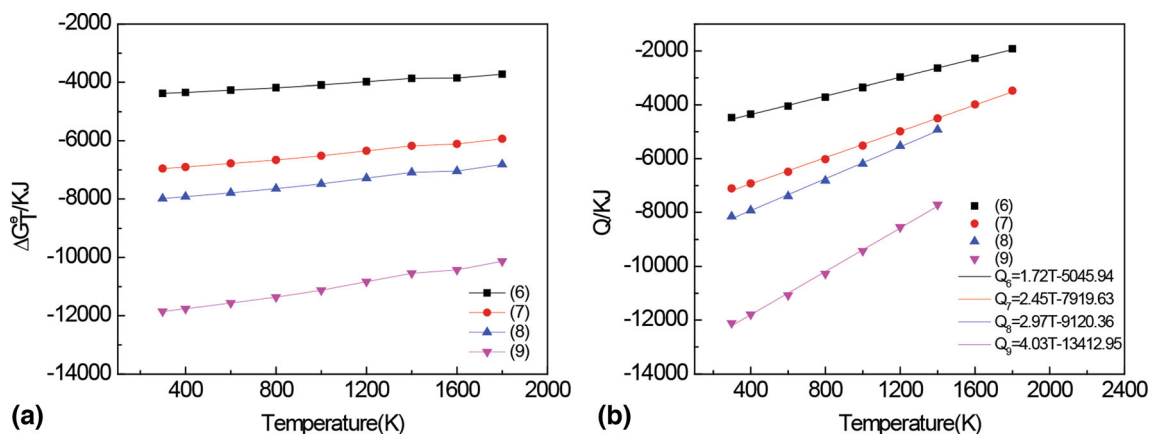
**Fig. 7** (a) Standard Gibbs free energy changes, (b) Q value with temperature of Eq. 6–9
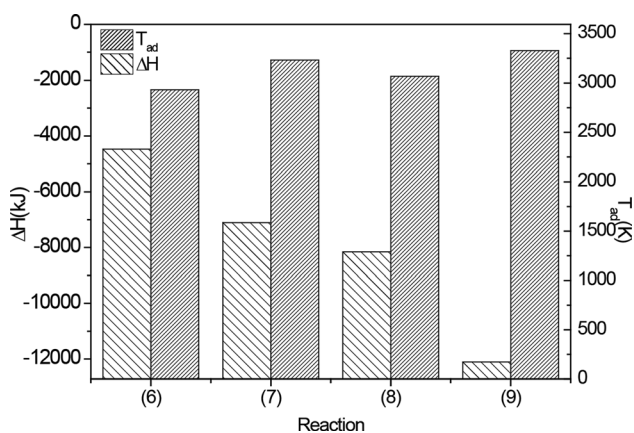


**Fig. 8** Enthalpy change ($\Delta H$) and adiabatic temperature ($T_{ad}$) of Eq. 6–9



**Fig. 9** DTA/TG curve of the $Cr_2O_3$-Al-$B_4C$ composite powder

self-propagating reaction can occur. The heat balance equation of the reaction in adiabatic condition is:

$$\Delta H_{298}^{\theta} + \sum n_I \left( H_T^{\theta} - H_{298}^{\theta} \right)_{i,\text{products}} = 0 \qquad (\text{Eq } 10)$$

$$Q = \Delta H_{298}^{\theta} + \sum n_I \left( H_T^{\theta} - H_{298}^{\theta} \right)_{i,\text{products}} \qquad (\text{Eq } 11)$$

Equation 10 has been rewritten as Eq. 11, where $Q$ represents the heat loss of the reaction system. When $Q$ is equal to 0, it indicates that the heat generated by the reaction is all used to heat the products, the system is in an adiabatic state, and the corresponding temperature is the adiabatic temperature. Figure 7(b) shows the trend of $Q$ with temperature, and $Q_6$–$Q_9$ are the fitting equations of the reaction waste heat, $Q$, with temperature for Eq. 6–9. If $Q = 0$, the adiabatic temperature $T_{ad}$ can be estimated. The calculation results are shown in Fig. 8, demonstrating that the adiabatic temperature of the four reactions is greater than 1800 K, indicating that the reactions can occur thermodynamically.

Figure 9 shows the DTA/TG curve of the $Cr_2O_3$-Al-$B_4C$ composite powder. It can be seen from the DTA curve that
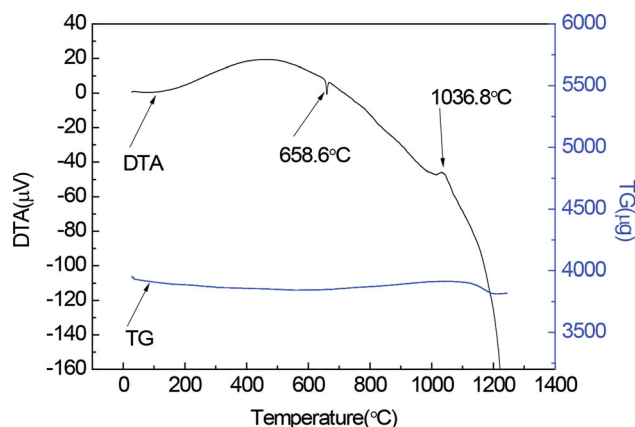
there is an endothermic peak near 658.6 °C. Considering that the melting point of Al is 660 °C, it is considered that the endothermic peak represents the melting of Al. When the temperature rose to about 1036.8 °C, an exothermic peak appeared in the DTA curve, indicating that an exothermic reaction occurred between the raw powders near this temperature. In the initial heating stage, due to the volatilization of the adhesive and water in the composite powder, the TG curve decreased slightly. With the continuous rise of temperature, there is a slight oxidation phenomenon in the composite powder. Therefore, the TG curve increased slightly, but the change degree of the curve was very small, indicating that the oxidation degree was very weak.

In order to further determine the phase transformation of the $Cr_2O_3$-Al-$B_4C$ composite powder during heating, according to DTA/TG curve, three heating temperatures of 700, 900, and 1100 °C were selected for heating, and then the phase analysis of the treated powder was carried out. The results are shown in Fig. 10. It can be seen from Fig. 10(a) that the phase of the composite powder treated at 700 °C is the same as that of the untreated composite
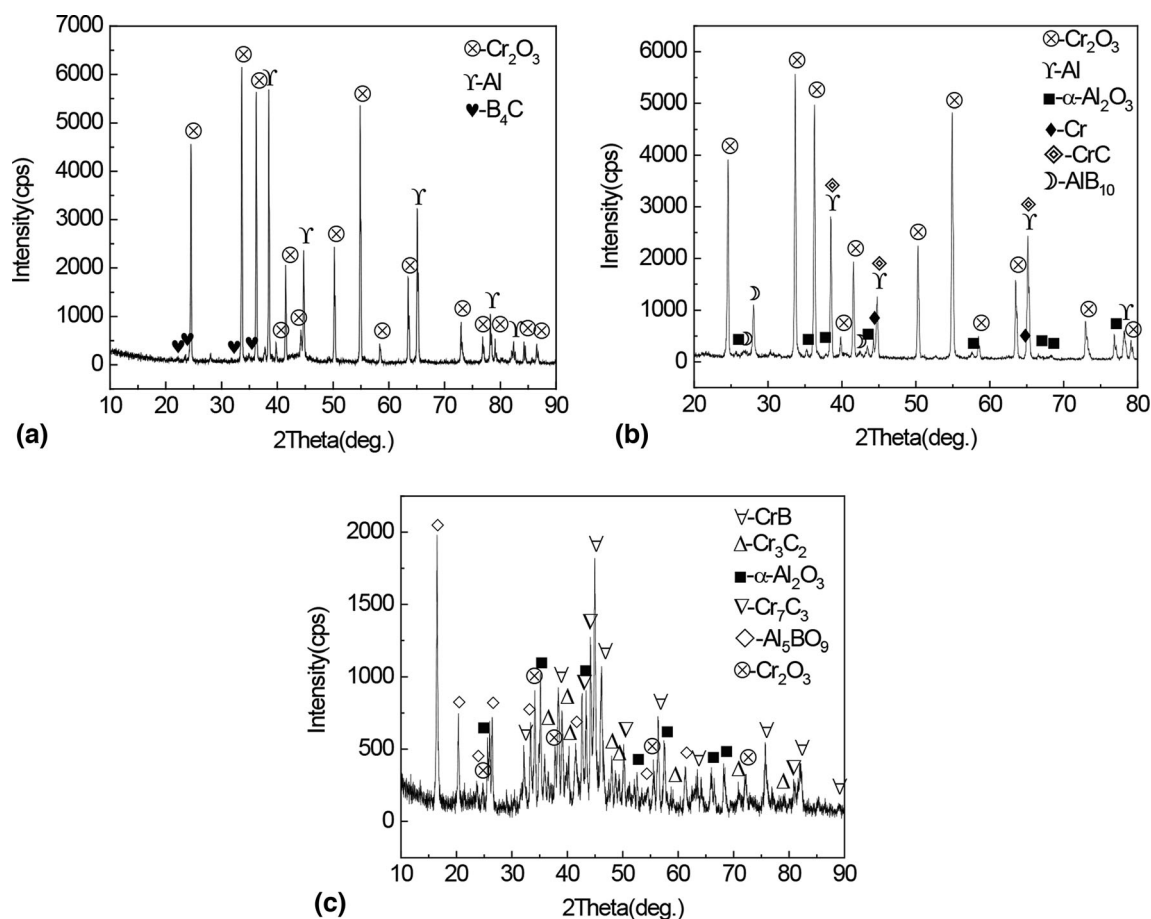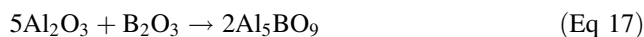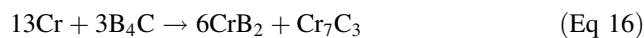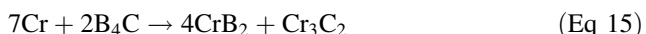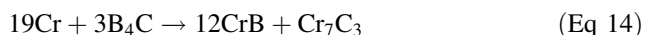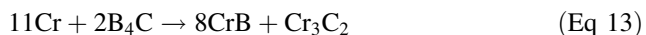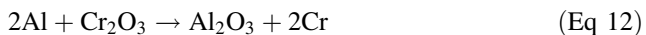
**Fig. 10** XRD patterns of the $Cr_2O_3$-Al-$B_4C$ composite powder heat treated at different temperatures: (a) 700 °C, (b) 900 °C, (c) 1100 °C

powder, indicating that the components in the composite powder did not react below 700 °C. The XRD of the composite powder treated at 900 °C is shown in Fig. 10(b). At this time, new phases of α-$Al_2O_3$, Cr, CrC, and $AlB_{10}$ appeared in the composite powder, indicating that the thermite reaction between $Cr_2O_3$ and Al began between 700 and 900 °C (Eq. (12)), and part of $B_4C$ was decomposed. The XRD of the composite powder treated at 1100 °C is shown in Fig. 10(c). At this time, the Al phase disappeared, indicating the end of the thermite reaction. In addition, the CrB, $Cr_3C_2$, and $Cr_7C_3$ phases were formed, indicating that the Cr generated by the reaction may further react with $B_4C$ (see Eq. 13–16). The formation of $Al_5BO_9$ may be attributed to the reaction of $B_2O_3$ formed by the oxidation of $B_4C$ and $Al_2O_3$, as shown in Eq. 17:

$$2Al + Cr_2O_3 \rightarrow Al_2O_3 + 2Cr \qquad (Eq\ 12)$$

$$11Cr + 2B_4C \rightarrow 8CrB + Cr_3C_2 \qquad (Eq\ 13)$$

$$19Cr + 3B_4C \rightarrow 12CrB + Cr_7C_3 \qquad (Eq\ 14)$$

$$7Cr + 2B_4C \rightarrow 4CrB_2 + Cr_3C_2 \qquad (Eq\ 15)$$

$$13Cr + 3B_4C \rightarrow 6CrB_2 + Cr_7C_3 \qquad (Eq\ 16)$$

$$5Al_2O_3 + B_2O_3 \rightarrow 2Al_5BO_9 \qquad (Eq\ 17)$$

In order to quantitatively analyze the contribution of the heat released from the thermite reaction to the melting of the compounds, the heat required for the melting of the products in Eq. 12 and the reactant in Eq. 13 was calculated, resulting in:

$$Q = \sum \left( n_I C_p (T_{melt} - T_0) + H \right) \qquad (Eq\ 18)$$

where $n_I$ is the stoichiometric number of the compound, $C_p$ is the average molar heat capacity of the compound from the melting point to room temperature, $T_{melt}$ is the melting point of the compound, $t_0$ is room temperature, and $H$ is the phase transition enthalpy of the compound. The results show that the heat required to melt $Cr_2O_3$ and Al is 509.255 kJ, the heat required to melt Cr and $B_4C$ is 1597.05 kJ, the heat released by Eq. 12 is 545.594 kJ, and the heat released by Eq. 15 is 327.608 kJ. Therefore, the superposition of the heat released by reaction and the heat provided by plasma jet is enough to melt $Cr_2O_3$, Al, and $B_4C$.

According to the results of thermodynamic analysis and thermal analysis, the reaction mechanism of $Cr_2O_3$-Al-$B_4C$ composite powder in the process of plasma spraying is speculated to be: firstly, compared with $Cr_2O_3$ and $B_4C$, Al with a lower melting point first melted to form a melt, which wrapped $Cr_2O_3$ and $B_4C$ particles; secondly, Al melt reacted with $Cr_2O_3$ particles to form Cr and $Al_2O_3$, and Cr, $Al_2O_3$ , and $B_4C$ were melted by the heat of thermite reaction and plasma jet; then, Cr and $B_4C$ reacted to form chromium boride and chromium carbide phases.

## Formation Mechanism of the Two Chromium Boride–Chromium Carbide–Alumina Composite Coatings

The observation of the deposition morphology of powder droplets during plasma spraying is beneficial to the understandng of the formation process of the coating. Figure 11(a) shows the SEM morphology of a single droplet after deposition of the $CrB_2$-$Cr_3C_2$-$Al_2O_3$ composite powder on the substrate. The droplet-sputtering morphology is obviously disc-shaped. There are obvious finger protrusions at the edge of the droplet and a large void inside the droplet, and the droplet surface is uneven. Figure 11(b) shows an enlarged view of a local area in Fig. 11(a), from which it can be seen that there are more unmelted particles in the droplet. Figure 11(c) shows the spreading morphology of a single droplet obtained by plasma spraying the $Cr_2O_3$-Al-$B_4C$ composite powder. It

can be seen that the droplet surface is relatively flat, there are almost no unmelted particles in the droplet, and there are no massive structures or obvious large defects in the droplet. Figure 11(d) is an enlarged view of a local area in Fig. 11(c), which shows that the droplet structure is uniform and dense. These results show that, compared with the $CrB_2$-$Cr_3C_2$-$Al_2O_3$ composite powder, the $Cr_2O_3$-Al-$B_4C$ composite powder showed a better melting and flattening degree and a higher cooling rate in the plasma jet, which is conducive to the formation of a more dense nanocrystalline structure during the deposition process ofthe coating.

A schematic of the formation mechanism of the coating prepared by plasma spraying the $CrB_2$-$Cr_3C_2$-$Al_2O_3$ composite powder is shown in Fig. 12(a). The formation process of the composite coating mainly includes two stages: melting and deposition of feedstocks. The specific process is as follows: the raw materials in the composite powders were mechanically combined under the action of the binder. After the composite powders were fed into the plasma jet, the nano-$Al_2O_3$ particles first melted to form the form of molten $Al_2O_3$ wrapping the $CrB_2$ and $Cr_3C_2$ particles. In the subsequent heating process, some $Cr_3C_2$ and $CrB_2$ particles began to melt, and the molten droplets wrapped unmelted particles. In the deposition process, under the carrier of the high-speed plasma jet, the melted droplets and unmelted raw powders impacted the substrate surface. Molten and semi-molten $CrB_2$ and $Cr_3C_2$ were deposited on the substrate surface, and the irregular block structure in

**Fig. 11** SEM micrographs of the splat of the two composite coatings: (a) $CrB_2$-$Cr_3C_2$-$Al_2O_3$, (b) partial amplification of (a), (c) $Cr_2O_3$-Al-$B_4C$, (d) partial amplification of (c)
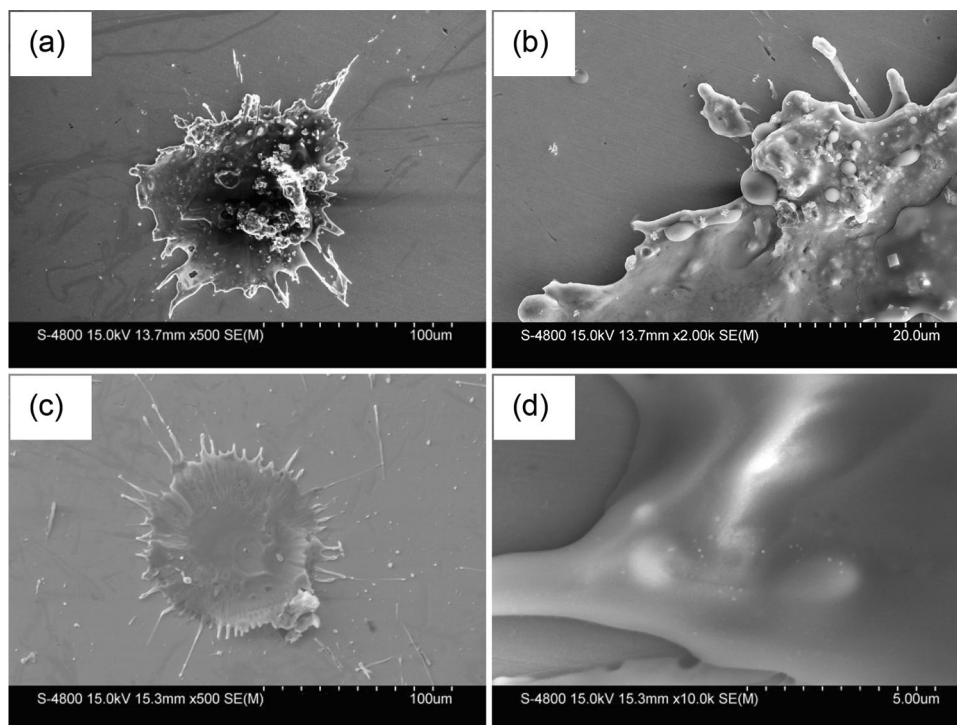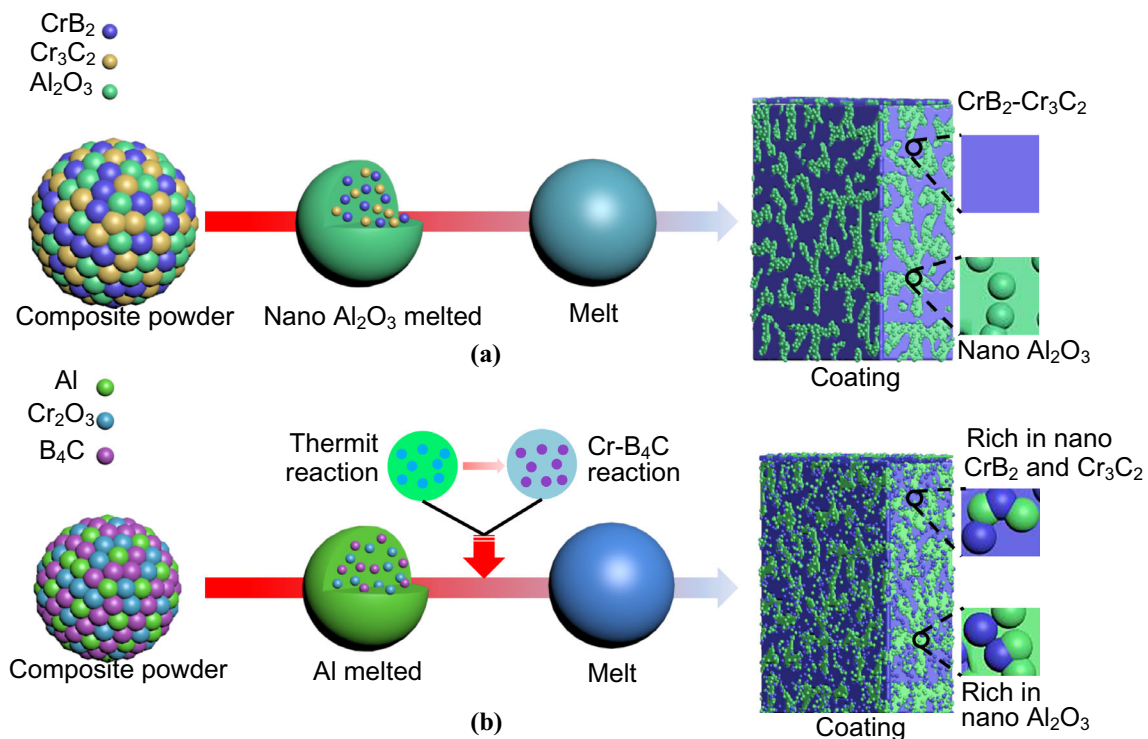
**Fig. 12** Schematic of the formation mechanism of the composite coatings: (a) $CrB_2$-$Cr_3C_2$-$Al_2O_3$, and (b) $Cr_2O_3$-Al-$B_4C$

the coating was formed after cooling, while $Al_2O_3$ with good melting state impacted and spread around the $CrB_2$ and $Cr_3C_2$ phases to form the lamellar structure in the coating. It can be seen that the microstructure of the coating obtained by plasma spraying the $CrB_2$-$Cr_3C_2$-$Al_2O_3$ composite powder was simple mechanical stacking, resulting in the high porosity of the composite coating.

Based on the analysis of the reaction mechanism and droplet spreading morphology of the $Cr_2O_3$-Al-$B_4C$ composite powder, the formation mechanism of the coating prepared by plasma spraying the powder is shown in Fig. 12(b). After the composite powders were fed into the plasma jet, the first stage was that the Al particles melted and wrapped outside the $Cr_2O_3$ and $B_4C$ particles, thus the contact area between raw materials was increased. In the second stage, with the continuous increase of temperature, a thermite reaction occurred between the molten Al and $Cr_2O_3$ to generate Cr and $Al_2O_3$. The generated Cr and $Al_2O_3$ were fully melted by the superposition of heat released from the thermite reaction and the heat of plasma jet, so the liquid environment for subsequent reactions was formed. In the third stage, Cr generated by the thermite reaction reacted with $B_4C$. The large amount of heat released by the $Cr_2O_3$-Al-$B_4C$ composite powder in the reaction process can fully melt the generated $CrB_2$, CrB, $Cr_3C_2$ , and $Cr_7C_3$. The fourth stage was the deposition

process. The molten products were carried by the high-speed jet and impacted the substrate surface. A relatively dense composite coating was formed after cooling.

## Properties of the Two Chromium Boride–Chromium Carbide–Alumina Composite Coatings

### Microhardness

The microhardness is an important index to characterize the properties of ceramic coatings. The microhardness of the coatings prepared by plasma spraying the $CrB_2$-$Cr_3C_2$-$Al_2O_3$ and $Cr_2O_3$-Al-$B_4C$ composite powders are $1057 \pm 138$ $HV_{0.1}$ and $1230 \pm 115$ $HV_{0.1}$, respectively. As an effective method to evaluate the mechanical properties of materials (Ref 42), the Weibull distribution of hardness can objectively and truly reflect the relationship between the mechanical properties and the microstructure of coatings. The Weibull distribution curve of microhardness of two composite coatings is shown in Fig. 13. The expression of the fitting line in the figure is:

$$y = mx + a \qquad \text{(Eq 19)}$$

where the larger the $m$ value, the lower the dispersion of the microhardness value and the more stable the performance. Compared with the coating prepared by plasma spraying the $CrB_2$-$Cr_3C_2$-$Al_2O_3$ composite powder, the

coating prepared by plasma spraying the $Cr_2O_3$-Al-$B_4C$ composite powder exhibits higher average microhardness and less dispersion. This can be attributed to two reasons. One is that the porosity of the coating obtained by plasma spraying the $Cr_2O_3$-Al-$B_4C$ composite powder is lower, and the lower the porosity, the higher the microhardness (Ref 43). Due to the phases in the coating prepared by plasma spraying the $Cr_2O_3$-Al-$B_4C$ composite powder being formed by in situ reaction and the thermite reaction resulting in the higher melting degree of the composite powder in the plasma jet, the coating microstructure uniformity is good, and thus the dispersion of the microhardness value is lower. Secondly, there are many in situ-formed nanocrystalline structures in the coating obtained by plasma spraying the $Cr_2O_3$-Al-$B_4C$ composite powder, which play a key role in the fine grain strengthening.



**Fig. 13** Microhardness Weibull distribution curves of the two $CrB_2$ composite coatings

## Toughness

Vickers indentation is one of the important methods to characterize the toughness of coatings (Ref 44, 45). Figure 14 shows the indentation morphology of the two composite coatings under a load of 300 g. The SEM micrograph of the indentation morphology of the coating prepared by plasma spraying the $CrB_2$-$Cr_3C_2$-$Al_2O_3$ composite powder is shown in Fig. 14(a), from which it can be seen that small cracks appeared in and around the indentation, and that there is no obvious warpage. The SEM micrograph of the indentation morphology of the coating prepared by plasma spraying the $Cr_2O_3$-Al-$B_4C$ composite powder is shown in Fig. 14(b), from which it can be seen that the indentation is relatively complete, and that there are no obvious cracks inside and around the indentation. Compared with the coating prepared by plasma spraying the $CrB_2$-$Cr_3C_2$-$Al_2O_3$ composite powder, the coating prepared by plasma spraying the $Cr_2O_3$-Al-$B_4C$ composite powder shows a better toughness, which may be attributed to fewer defects such as pores and to the nanocrystalline structure in the $Cr_2O_3$-Al-$B_4C$ composite coating.

The fracture morphology of the composite coating can to a certain extent reflect the microstructure of the coating. At the same time, the fracture toughness can be judged by observing the fracture step and the propagation mode of the crack. The larger the fracture fluctuation, the more complex the crack propagation path. The more energy the material consumes in the fracture process, the higher the strength and toughness of the material. Figure 15 shows the fracture morphology of the composite coatings of the two systems, in which the coating prepared by plasma spraying the $CrB_2$-$Cr_3C_2$-$Al_2O_3$ composite powder is shown in Fig. 15(a), (c), and (e) and the coating prepared by plasma spraying the $Cr_2O_3$-Al-$B_4C$ composite powder is shown in Fig. 15(b), (d), and (f). Comparing Fig. 15(a) with (b), it can be seen that the fracture morphology of the coatings of the two systems shows obvious brittle fracture characteristics. The lamellar distribution of the microstructure in the coating prepared by plasma spraying the $CrB_2$-$Cr_3C_2$-
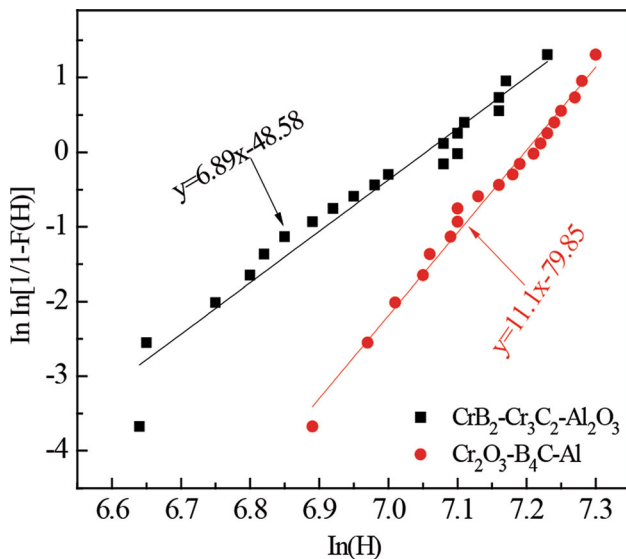
**Fig. 14** SEM micrographs of surface indentation of the composite coatings: (a) $CrB_2$-$Cr_3C_2$-$Al_2O_3$, and (b) $Cr_2O_3$-Al-$B_4C$
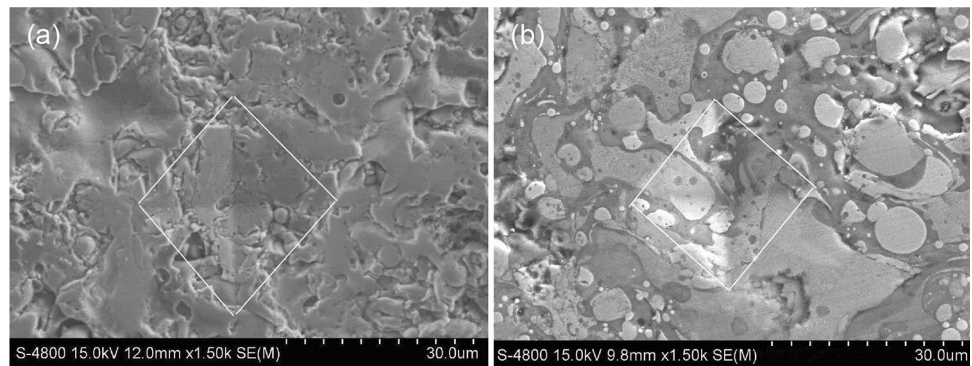
**Fig. 15** SEM micrographs of the fracture surfaces of the composite coatings: (a) $CrB_2$-$Cr_3C_2$-$Al_2O_3$; (b) $Cr_2O_3$-Al-$B_4C$; (c) and (e) are enlarged views of partial areas of the $CrB_2$-$Cr_3C_2$-$Al_2O_3$ system; (d) and (f) are enlarged views of partial areas of the $Cr_2O_3$-Al-$B_4C$ system
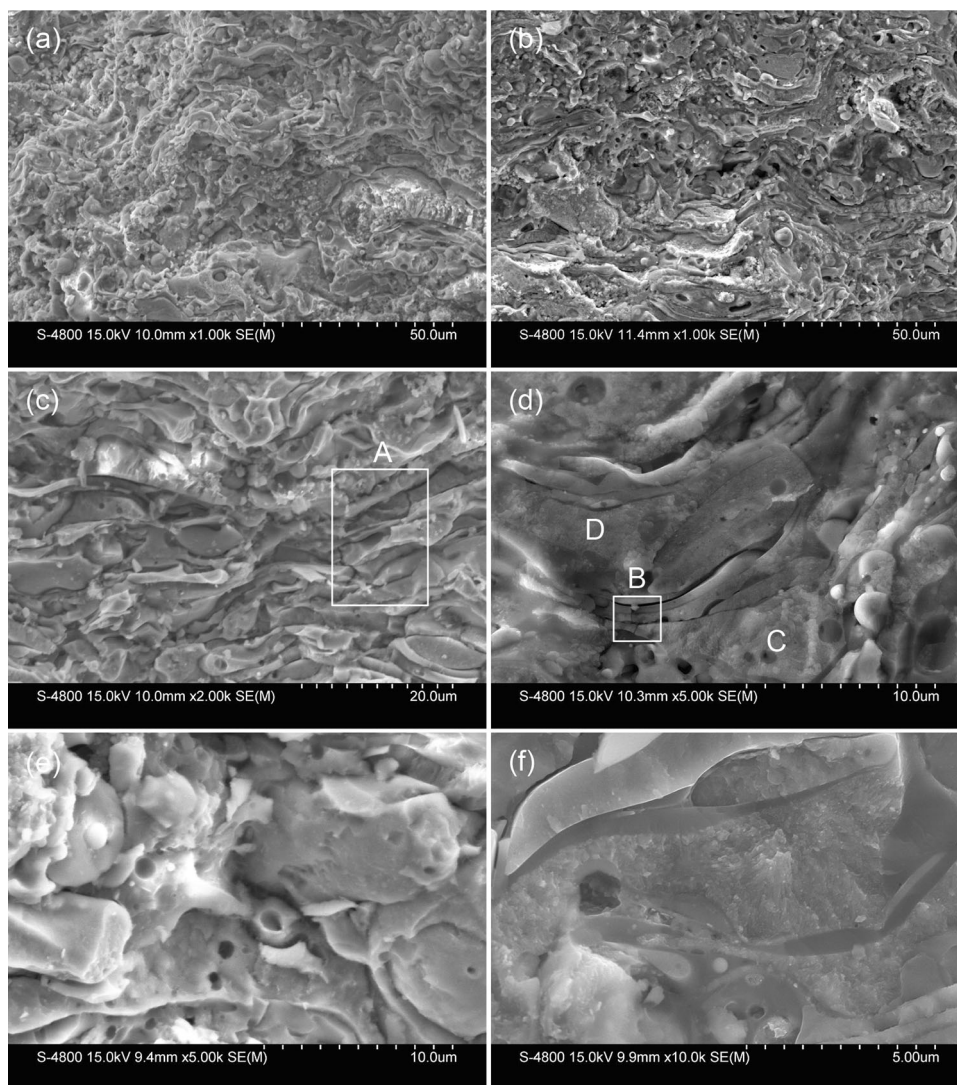


$Al_2O_3$ composite powder is not obvious, and the microstructure is mainly in the bulk distribution, while the coating prepared by plasma spraying the $Cr_2O_3$-Al-$B_4C$ composite powder displays obvious a lamellar microstructure and the fracture fluctuates. A long crack is found in area A in Fig. 15(c), which started from the lamellar gap and passed through multiple lamellae during the propagation process, indicating that the coating had poor crack propagation resistance. As can be seen from Fig. 15(d), there are small cracks in area B, but the cracks terminated in a single layer and did not pass between the layers, showing that the coating prepared by plasma spraying the $Cr_2O_3$-Al-$B_4C$ composite powder had a good ability to resist crack propagation. From regions C and D, it can be found that there are many nanoparticles inside the lamellae, and that the microstructure is obviously refined. As can be seen from Fig. 15(e), there is no nanosized structure in the lamellae of the coating prepared by plasma

spraying the $CrB_2$-$Cr_3C_2$-$Al_2O_3$ composite powder. As shown in Fig. 15(f), in the coating prepared by plasma spraying the $Cr_2O_3$-Al-$B_4C$ composite powder, the microstructure formed in situ is uniform and dense, and the phase interface is pure, which can result in a higher interface bonding strength, which is conducive to improving the crack propagation energy. It is speculated that the good crack propagation resistance of the coating prepared by plasma spraying the $Cr_2O_3$-Al-$B_4C$ composite powder may be attributed to the formation of a nanolamellar structure. Therefore, compared with the coating prepared by plasma spraying the $CrB_2$-$Cr_3C_2$-$Al_2O_3$ composite powder, the coating prepared by plasma spraying the $Cr_2O_3$-Al-$B_4C$ composite powder shows a better toughness.

## Scratch Resistance

The scratch resistance of a coating refers to the ability of the coating surface to resist damage and deformation under a certain normal load. When the load reaches a critical state of coating cracking, cracks occur. At this time, a large strain energy is released inside the coating, and the resulting elastic fluctuation is collected by the acoustic emission equipment, showing a large strength on the signal curve (Ref 46). Figure 16 shows the acoustic emission signals detected by the composite coatings during the scratch process. As can be seen from Fig. 16(a), when the load was 19.9 N, a strong signal fluctuation was detected by acoustic emission, indicating that cracks had begun to appear on the surface of the coating prepared by plasma spraying the $CrB_2$-$Cr_3C_2$-$Al_2O_3$ composite powder. With the increase of the load, the signal fluctuation gradually increased, indicating that the cracks on the coating surface continued to expand and increase. As can be seen from Fig. 16(b), when the load was increased to 40.5 N, a strong signal fluctuation was detected by acoustic emission, indicating that microcracks had begun to appear on the surface of the coating prepared by plasma spraying the $Cr_2O_3$-Al-$B_4C$ composite powder at this time. With the increase of the load, the signal fluctuation was less, indicating that the number of cracks on the surface of coating prepared by plasma spraying the $Cr_2O_3$-Al-$B_4C$ composite powder was less. Compared with the coating prepared by plasma spraying the $CrB_2$-$Cr_3C_2$-$Al_2O_3$ composite powder, the coating prepared by plasma spraying the $Cr_2O_3$-Al-$B_4C$ composite powder exhibited a greater critical load and better scratch resistance.

Figure 17(a) and (b) shows the morphology SEM micrographs of the scratch end of the two chromium boride–chromium carbide–alumina composite coating after the scratch tests, respectively. Compared with the coating prepared by plasma spraying the $CrB_2$-$Cr_3C_2$-$Al_2O_3$ composite powder, the scratch depth of the coating prepared by plasma spraying the $Cr_2O_3$-Al-$B_4C$ composite powder is relatively shallow and the scratch width is narrow, indicating that the damage of the indenter to the coating prepared by plasma spraying the $Cr_2O_3$-Al-$B_4C$ composite powder was not obvious during the scratch process. Figure 17(c) shows a partial enlarged view of Fig. 17(a). It can be seen that the scratch surface structure is loose, the bonding strength of the phase interface is low, and the cracks are easy to propagate through the phase interface, so that many cracks are generated perpendicular to the scratch direction. Figure 17(d) is a partial enlarged view of Fig. 17(b), from which it can be seen that the scratch surface is still dense. Although cracks are also found, the number and length of the cracks are smaller than in Fig. 17(c). In addition, deflection (region A) and bifurcation (region B) of the cracks can be seen on the scratch surface. Combined with the acoustic emission curve of the composite coatings, the scratch resistance of the coating prepared by plasma spraying the $Cr_2O_3$-Al-$B_4C$ composite powder is better than that of the coating prepared by plasma spraying the $CrB_2$-$Cr_3C_2$-$Al_2O_3$ composite powder. The microstructure is the main factor affecting the scratch resistance of the coating. The higher the content of the hard phase in the coating, the denser the structure, the higher the hardness, and the better the scratch resistance of the coating (Ref 47, 48). Combined the cross-sectional morphology with the toughness analysis of the composite coating, the coating prepared by plasma spraying the $Cr_2O_3$-Al-$B_4C$ composite powder has excellent compactness, a more refined microstructure, and high hardness and toughness. Therefore, the scratch resistance of the coating prepared by plasma spraying the $Cr_2O_3$-Al-$B_4C$ composite powder is better than that of the coating prepared by plasma spraying the $CrB_2$-$Cr_3C_2$-$Al_2O_3$ composite powder.



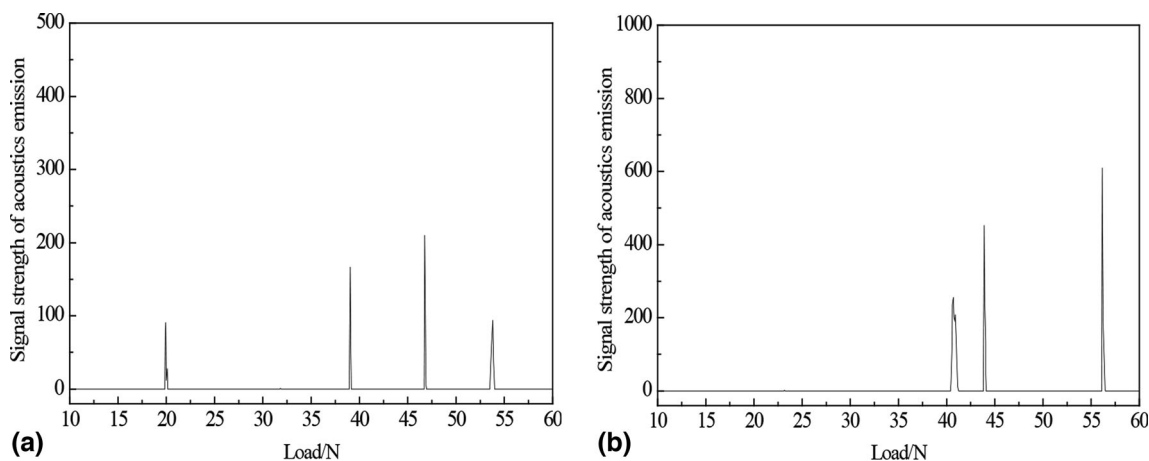**Fig. 16** Acoustic emission signals of the composite coatings: (a) $CrB_2$-$Cr_3C_2$-$Al_2O_3$; (b) $Cr_2O_3$-Al-$B_4C$

Fig. 17 End sections of scratches of the coatings prepared by plasma spraying the composite powders: (a) $CrB_2$-$Cr_3C_2$-$Al_2O_3$, and (b) $Cr_2O_3$-Al-$B_4C$, (c) is a enlarged view of partial areas of (a), (d) is a enlarged view of partial areas of (b)
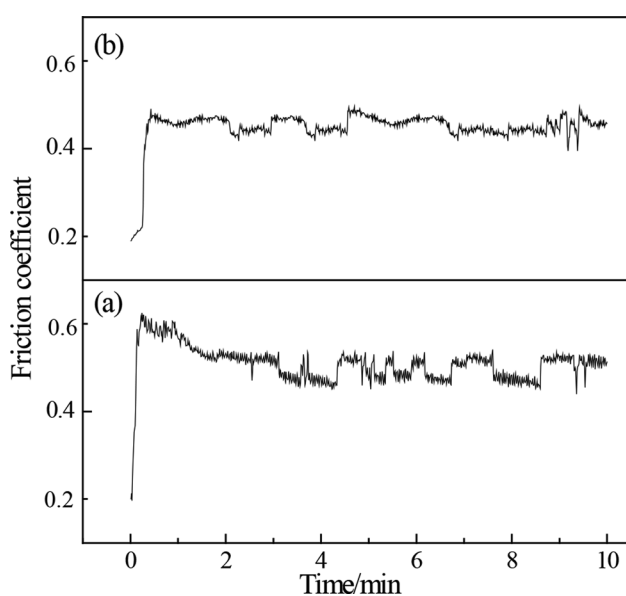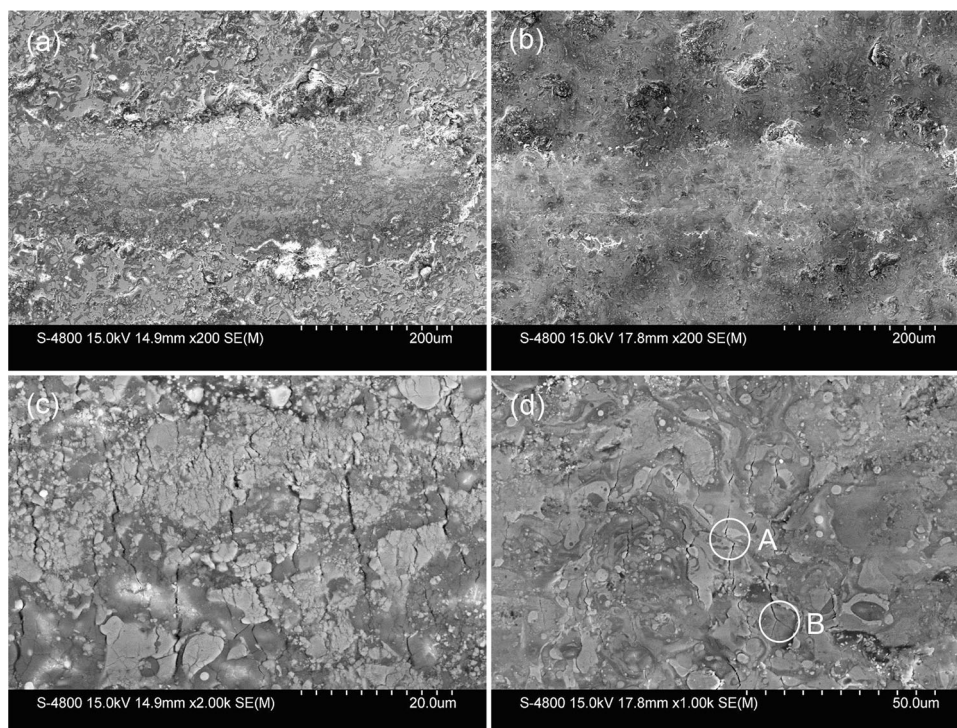




Fig. 18 Friction coefficient curves of the two composite coatings: (a) $CrB_2$-$Cr_3C_2$-$Al_2O_3$, and (b) $Cr_2O_3$-Al-$B_4C$

Fig. 19 Wear profile of the two composite coatings

## Sliding Wear Resistance

The friction coefficient curve of two composite coatings is shown in Fig. 18. It can be seen that the variation trend of the friction coefficient of the two composite coatings first increases and then tends to be stable. The average friction coefficients of the coatings prepared by plasma spraying the $CrB_2$-$Cr_3C_2$-$Al_2O_3$ and $Cr_2O_3$-Al-$B_4C$ composite

powders are 0.51 and 0.445, respectively. The coating prepared by plasma spraying the $CrB_2$-$Cr_3C_2$-$Al_2O_3$ composite powder has high porosity, more unmelted particles, and more surface microdefects. The coating prepared by plasma spraying the $Cr_2O_3$-Al-$B_4C$ composite powder has a more uniform and dense structure and relatively low porosity, so the coating surface is smoother and the coating is not easy to peel off during friction with the friction pair. Therefore, the friction coefficient of the coating prepared by plasma spraying the $CrB_2$-$Cr_3C_2$-$Al_2O_3$ composite

powder is higher than that of the coating prepared by plasma spraying the $Cr_2O_3$-Al-$B_4C$ composite powder.

The wear scar of two composite coatings is shown in Fig. 19, from which it can be seenthat the wear scar of the coating prepared by plasma spraying the $Cr_2O_3$-Al-$B_4C$ composite powder is shallower than that of the coating prepared by plasma spraying the $CrB_2$-$Cr_3C_2$-$Al_2O_3$ composite powder. The wear rate of the coatings prepared by plasma spraying the $CrB_2$-$Cr_3C_2$-$Al_2O_3$ and $Cr_2O_3$-Al-$B_4C$ composite powders calculated by Eq. 1 are $0.98 \times 10^{-3}$ and $0.72 \times 10^{-3}$ $mm^3$/N m, respectively. It can be seen that the wear rate of the coating prepared by plasma spraying the $CrB_2$-$Cr_3C_2$-$Al_2O_3$ composite powder is higher than that of the coating prepared by plasma spraying the $Cr_2O_3$-Al-$B_4C$ composite powder because the porosity of the coating prepared by plasma spraying the $CrB_2$-$Cr_3C_2$-$Al_2O_3$ composite powder is relatively high. There are many surface microdefects, and the bonding strength of each layer in the coating is low. In the process of friction, the friction stress can very easily exceed the bonding strength between the layers, resulting in easy peeling of the coating. Therefore, the overall wear of the coating increases. The coating prepared by plasma spraying the $Cr_2O_3$-Al-$B_4C$ composite powder synthesized by the in situ reaction has a lower porosity, a more refined microstructure, and higher microhardness. Therefore, the wear performance of the coating prepared by plasma spraying the $Cr_2O_3$-Al-$B_4C$ composite powder is better than that of the coating prepared by plasma spraying $CrB_2$-$Cr_3C_2$-$Al_2O_3$ composite powder.

The wear scar morphology of two composite coatings is shown in Fig. 20. Comparing Fig. 20(a) and (b), for the coating prepared by plasma spraying the $CrB_2$-$Cr_3C_2$-$Al_2O_3$ composite powder, the width of the wear scar is relatively large and the wear scar surface is relatively rough, while the width of the wear scar of the coating prepared by plasma spraying the $Cr_2O_3$-Al-$B_4C$ composite powder is more small and the wear scar surface is more smooth. Figure 20(c) is an enlarged view of the middle area of the wear scar in Fig. 20(a), which shows that the wear scar surface has obvious smooth areas and rough areas, the smooth area being the deformation layer generated by the friction between the ceramic ball and the dense structure in the coating, and the rough area being the pores in the coating or the peeling pits caused by the wear (Ref 49). Figure 20(c') is an enlarged view of the edge area of the wear scar in Fig. 20(a). It can be seen that this area is mainly composed of loose particles, indicating that the coating is seriously worn. Figure 20(d) is an enlarged view of the local area in Fig. 20(b), from which it can be seen that the smooth area of the wear scar surface has obvious tissue deformation, but there is still no large lamellar spalling, while the peeling pit area of the rough area is small. Compared with the coating prepared by plasma spraying the $CrB_2$-$Cr_3C_2$-$Al_2O_3$ composite powder, the coating prepared by plasma spraying the $Cr_2O_3$-Al-$B_4C$



**Fig. 20** SEM micrographs of wear scars of the two composite coatings: (a), (c) $CrB_2$-$Cr_3C_2$-$Al_2O_3$; (b), (d) $Cr_2O_3$-Al-$B_4C$
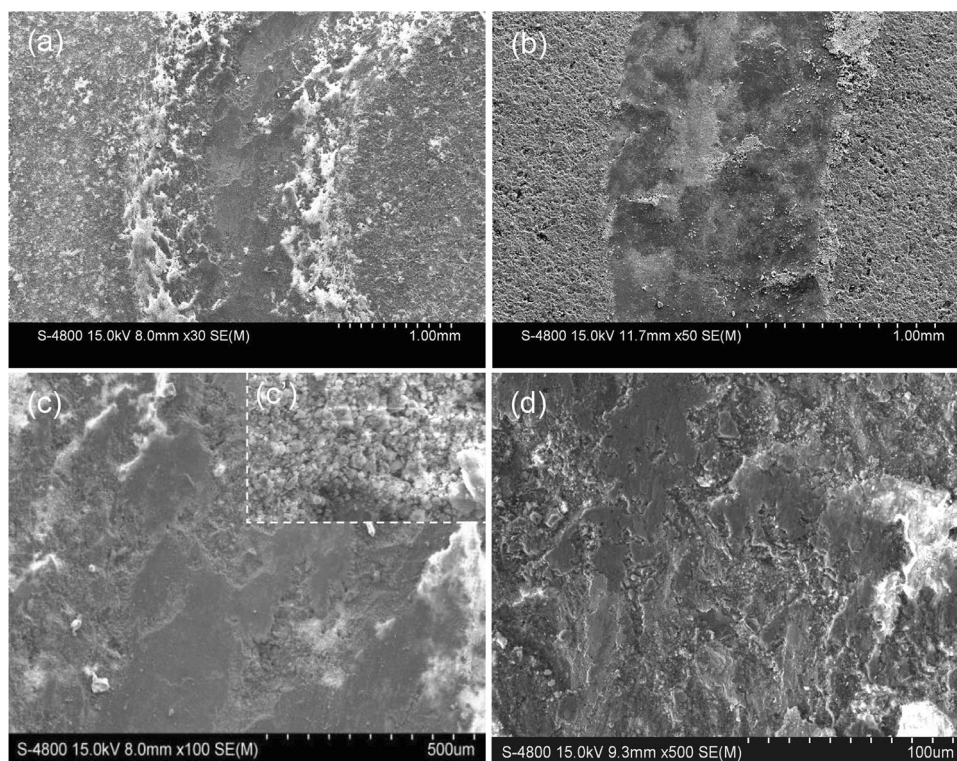
composite powder does not have large lamellar spalling. The possible explanation is that the coating shows an obvious refined microstructure and high toughness. In the process of friction and wear, the coating has high deformation resistance, difficult crack propagation, and is not easy to fracture. Table 3 shows the data of microhardness, coefficient of friction, and wear rate of the composite coatings containing chromium boride or chromium carbide prepared by plasma spraying. It can be seen that, compared with the composite coatings reported in the literatures, the $CrB_2$-$Cr_3C_2$-$Al_2O_3$ composite coating synthesized in situ by plasma spraying the $Cr_2O_3$-Al-$B_4C$ composite powder in this work shows a higher microhardness and a lower coefficient of friction and wear rate, displaying excellent wear resistance.

## Conclusions

(1) The coating prepared by plasma spraying the $CrB_2$-$Cr_3C_2$-$Al_2O_3$ composite powder consisted of $CrB_2$, CrB, $Cr_3C_2$, $\alpha$-$Al_2O_3$, and $\gamma$-$Al_2O_3$. The coating prepared by plasma spraying the $Cr_2O_3$-Al-$B_4C$ composite powder was composed of $CrB_2$, CrB, $Cr_3C_2$, $Cr_7C_3$, and $\gamma$-$Al_2O_3$. The results show that the composite coatings mainly composed of chromium boride and chromium carbide can be prepared in situ by plasma spraying $Cr_2O_3$-Al-$B_4C$ composite powder.

(2) The coating prepared by plasma spraying the $CrB_2$-$Cr_3C_2$-$Al_2O_3$ composite powder had many pores and an uneven microstructure. The microstructure of the composite coating prepared in situ by plasma spraying the $Cr_2O_3$-Al-$B_4C$ composite powder was obviously lamellar and refined, many nanosized chromium boride and chromium carbide phases were formed, the in situ-formed phases were closely bonded, and the porosity of the coating was low.

(3) The formation mechanism of the coating prepared by plasma spraying the $CrB_2$-$Cr_3C_2$-$Al_2O_3$ composite powder is a melting–deposition mechanism. The formation mechanism of the coating obtained by plasma spraying the $Cr_2O_3$-Al-$B_4C$ composite powder includes three stages: melting, reaction, and deposition. Al powders with a low melting point melted and wrapped the $Cr_2O_3$ and $B_4C$ particles. Then, an in situ reaction occurred which was divided into two steps. First, Al and $Cr_2O_3$ underwent a thermite reaction to form Cr and $Al_2O_3$ phases, and second, Cr and $B_4C$ reacted to form chromium boride and chromium carbide phases.

(4) The average microhardness of the coating prepared by plasma spraying the $CrB_2$-$Cr_3C_2$-$Al_2O_3$

composite powder was $1057 \pm 138$ $HV_{0.1}$, the microhardness dispersion was large, the friction coefficient was 0.51, and the wear rate was $0.98 \times 10^{-3}$ $mm^3$/N m. The microhardness of the coating obtained by plasma spraying the $Cr_2O_3$-Al-$B_4C$ composite powder was $1230 \pm 115$ $HV_{0.1}$, the hardness dispersion was small, the coefficient of friction was 0.445, and the wear rate was $0.72 \times 10^{-3}$ $mm^3$/N m. The coating obtained by plasma spraying the $Cr_2O_3$-Al-$B_4C$ composite powder exhibits obvious microstructure refinement, good toughness, scratch resistance, and sliding wear resistance.

## References

1. L.C. Zhang, L.Y. Chen, and L.Q. Wang, Surface Modification of Titanium and Titanium Alloys: Technologies, Developments, and Future Interests, *Adv. Eng. Mater.*, 2020, **22**, p 1901258.
2. V.V. Stolyarov, L.S. Shuster, M.S. Migranov, R.Z. Valiev and Y.T. Zhu, Reduction of Friction Coefficient of Ultrafine-Grained CP Titanium, *Mater. Sci. Eng. A.*, 2004, **371**, p 313-317.
3. L.Y. Zhang, C.T. Peng, X.W. Yao, Q.F. Guan and R.F. Lu, Surface Alloying of Cr on Ti6Al4V Alloy Induced by High-Current Pulse Electron Beam, *Surf. Coat. Technol.*, 2019, **370**, p 288-297.
4. Q. Liu, Y. Liu, X. Li and G.N. Dong, Pulse Laser-Induced Cell-Like Texture on Surface of Titanium Alloy for Tribological Properties Improvement, *Wear*, 2021, **477**, p 203784.
5. D. Tobola, J. Morgiel and L. Maj, TEM Analysis of Surface Layer of Ti-6Al-4V ELI Alloy After Slide Burnishing and Low-Temperature Gas Nitriding, *Appl. Surf. Sci.*, 2020, **515**, p 195942.
6. X.J. Cai, Y. Gao, F. Cai, L. Zhang and S.H. Zhang, Effects of Multi-Layer Structure on Microstructure, Wear and Erosion Performance of the Cr/CrN Films on Ti Alloy Substrate, *Appl. Surf. Sci.*, 2019, **483**, p 661-669.
7. A.M. Ma, D.X. Liu, C.B. Tang, X.H. Zhang and C.S. Liu, Influence of Glow Plasma Co-Based Alloying Layer on Sliding Wear and Fretting Wear Resistance of Titanium Alloy, *Tribol. Int.*, 2018, **125**, p 85-94.
8. T.G. Zhang, H.G. Zhuang, Q. Zhang, B. Yao and F. Yang, Influence of $Y_2O_3$ on the Microstructure and Tribological Properties of Ti Based Wear-Resistant Laser-Clad Layers on TC4 Alloy, *Ceram. Int.*, 2020, **46**, p 13711-13723.
9. F. Wang, H.J. Yu, C.Z. Chen, J.L. Liu, L.J. Zhao, J.J. Dai and Z.H. Zhao, Effect of Process Parameters on the Microstructure Evolution and Wear Property of the Laser Cladding Coatings on Ti-6Al-4V Alloy, *J. Alloys Compd.*, 2017, **692**, p 989-996.
10. Y.N. Liu, L.J. Yang, X.J. Yang, T.G. Zhang and R.L. Sun, Optimization of Microstructure and Properties of Composite Coatings by Laser Cladding on Titanium Alloy, *Ceram. Int.*, 2021, **47**, p 2230-2243.
11. J.W. Qi, Y.M. Yang, M.M. Zhou, Z.B. Chen and K. Chen, Effect of Transition Layer on the Performance of Hydroxyapatite/

Titanium Nitride Coating developed on Ti-6Al-4V Alloy by Magnetron Sputtering, *Ceram. Int.*, 2019, **45**, p 4863-4869.

12. X. Yao, X. Zhang, H. Wu, L. Tian, Y. Ma and B. Tang, Microstructure and Antibacterial Properties of Cu-Doped $TiO_2$ Coating on Titanium by Micro-Arc Oxidation, *Appl. Surf. Sci.*, 2014, **292**, p 944-947.

13. Q.Q. Guo, D.P. Xu, W. Yang, Y.C. Guo, Z. Yang, J.P. Li and P.H. Gao, Synthesis, Corrosion, and Wear Resistance of a Black Microarc Oxidation Coating on Pure Titanium, *Surf. Coat. Technol.*, 2020, **386**, p 125454.

14. R.B. Heimann, *Plasma-Spray Coating*, VCH Publishers, New York, NY, 1996.

15. Y. Wang, C.G. Li, W. Tian, and Y. Yang, Laser Surface Remelting of Plasma Sprayed Nanostructured $Al_2O_3$-13wt%$TiO_2$ Coatings on Titanium Alloy, *Appl. Surf. Sci.*, 2009, **225**, p 8603-8610.

16. I.D. Utu, G. Marginean, I. Hulka, V.A. Serban and D. Cristea, Properties of the Thermally Sprayed $Al_2O_3$-$TiO_2$ Coatings Deposited on Titanium Substrate, *Int. J. Refract. Met. Hard Mater.*, 2015, **51**, p 118-123.

17. L. Wang, S.Y. Liu, J.F. Gou, Q.W. Zhang, F.F. Zhou, Y. Wang and R.Q. Chu, Study on the Wear Resistance of Graphene Modified Nanostructured $Al_2O_3$/$TiO_2$ Coatings, *Appl. Surf. Sci.*, 2019, **492**, p 272-279.

18. F. Ghadami, M. Heydarzadeh Sohi and S. Ghadami, Effect of TIG Surface Melting on Structure and Wear Properties of Air Plasma-Sprayed WC-Co Coatings, *Surf. Coat. Technol.*, 2015, **261**, p 108-113.

19. Y.X. Du, H.F. Chen, G. Yang, B. Liu, Y.F. Gao and H.J. Luo, Effect of Cobalt Content on High-Temperature Tribological Properties of TiC-Co Coatings, *Ceram. Int.*, 2018, **44**, p 14186-14194.

20. S. Matthews, Development of High Carbide Dissolution/Low Carbon Loss $Cr_3C_2$-NiCr Coatings by Shrouded Plasma Spraying, *Surf. Coat. Technol.*, 2014, **258**, p 886-900.

21. Q. Liu, Y. Bai, H.D. Wang, G.Z. Ma, M. Liu, C.Y. Chu, Y.W. Sun, W. Fan, F. Ding, B. Zhao and Y.T. Wang, Microstructural Evolution of Carbides and its Effect on Tribological Properties of SAPS or HVOF Sprayed NiCr-$Cr_3C_2$ Coatings, *J. Alloys Compd.*, 2019, **803**, p 730-741.

22. V. Reddy, J.K. Sonber, K. Sairam, T.S.R.C. Murthy, S. Kumar, G.V.S.N. Rao, T.S. Rao and J.K. Chakravartty, Densification and Mechanical Properties of $CrB_2$-$MoSi_2$ Based Novel Composites, *Ceram. Int.*, 2015, **41**, p 7611-7617.

23. K. Hirota, K. Mitani, M. Yoshinaka and O. Yamaguchi, Simultaneous Synthesis and Consolidation of Chromium Carbides ($Cr_3C_2$, $Cr_7C_3$ and $Cr_{23}C_6$) by Pulsed Electric-Current Pressure Sintering, *Mater. Sci. Eng. A*, 2005, **399**, p 154-160.

24. O. Poliarus, J. Morgiel, P. Bobrowski, M. Szlezynger, O. Umanskyi, M. Ukrainets, L. Maj and O. Kostenko, Effect of Powder Preparation on the Microstructure and Wear of Plasma-Sprayed NiAl/$CrB_2$ Composite Coatings, *J. Therm. Spray Technol.*, 2019, **28**, p 1039-1048.

25. Y.W. Wang, X.W. Sun, L. Wang, Y. Yang, X.X. Ren, Y.D. Ma, Y.H. Cui, W.W. Sun, X.Y. Wang and Y.C. Dong, Microstructure and Properties of $CrB_2$-$Cr_3C_2$ Composite Coatings Prepared by Plasma Spraying, *Surf. Coat. Technol.*, 2021, **425**, p 127693.

26. J. Mei, R.D. Halldearn and P. Xiao, Mechanisms of the Aluminum-Iron Oxide Thermite Reaction, *Scripta Mater.*, 1999, **41**, p 541-548.

27. Y. Fang, X.H. Liu, Y.X. Feng, J.F. Zhu and W. Jiang, Microstructure and Mechanical Properties of $Ti_3$(Al, Ga)$C_2$/$Al_2O_3$ Composites Prepared by In Situ Reactive Hot Pressing, *J. Adv. Ceram.*, 2020, **9**(6), p 782-790.

28. C.L. Yeh and J.Z. Lin, Effects of Boron Source on Combustion Synthesis of Chromium Boride/$Al_2O_3$ Composites, *Mater. Manuf. Process.*, 2013, **28**, p 1335-1339.

29. C.L. Yeh and G.T. Liou, A Novel Route for Synthesis of Alumina-Chromium Carbide Composites from PTFE-Activated $Cr_2O_3$/Al/C Combustion, *Ceram. Int.*, 2018, **44**, p 19486-19491.

30. W. Zheng, J.M. Wu, S. Chen, C.S. Wang, C.L. Liu, S.B. Hua, K.B. Yu, J. Zhang, J.X. Zhang and Y.S. Shi, Influence of $Al_2O_3$ Content on Mechanical Properties of Silica-Based Ceramic Cores Prepared by Stereolithography, *J. Adv. Ceram.*, 2021, **10**(6), p 1381-1388.

31. X.Y. Wang, W. Yang, Y.X. Shao, Y. Yang, Z.L. Yang, Y.W. Wang, Y.H. Cui, Y.D. Ma, W.W. Sun and W. Li, Effect of Nano-$Al_2O_3$ on the Microstructure and Properties of $NbB_2$-NbC Composite Coatings Prepared by Plasma Spraying, *J. Am. Ceram. Soc.*, 2022, **105**, p 712-727.

32. M. Dai, X.M. Song, C.C. Lin, Z.W. Liu, W. Zheng and Y. Zeng, Investigation of Microstructure Changes in $Al_2O_3$-YSZ Coatings and YSZ Coatings and Their Effect on Thermal Cycle Life, *J. Adv. Ceram.*, 2022, **11**(2), p 345-353.

33. X.Q. Cao, R. Vassen, S. Schwartz, W. Jungen, F. Tietz and D. Stöever, Spray-Drying of Ceramics for Plasma-Spray Coating, *J. Eur. Ceram. Soc.*, 2000, **20**, p 2433-2439.

34. A. Godavarty, A. Agarwal and N.B. Dahotre, Neural Networks in Studies on Oxidation Behavior of Laser Surface Engineered Composite Boride Coatings, *Appl. Surf. Sci.*, 2000, **161**, p 131-138.

35. J.K. Sonber, T.S.R.C. Murthy, C. Subramanian, S. Kumar, R.K. Fotedar and A.K. Suri, Investigation on Synthesis, Pressureless Sintering and Hot Pressing of Chromium Diboride, *Int. J. Refract. Met. Hard Mater.*, 2009, **27**, p 912-918.

36. Y.D. Chen, Y. Yang, Z.H. Chu, X.G. Chen, L. Wang, Z. Liu, Y.C. Dong, D.R. Yan, J.X. Zhang and Z.L. Kang, Microstructure and Properties of $Al_2O_3$-$ZrO_2$ Composite Coatings Prepared by Air Plasma Spraying, *Appl. Surf. Sci.*, 2018, **431**, p 93-100.

37. J.R. Davis, *Handbook of Thermal Spray Technology*, ASM International, Materials Park, 2004.

38. H.M. Bian, Y. Yang, Y. Wang and W. Tian, Preparation of Nanostructured Alumina-Titania Composite Powders by Spray Drying, Heat Treatment and Plasma Treatment, *Powder Technol.*, 2012, **219**, p 257-263.

39. D.L. Ye and J.H. Hu, *Handbook of Thermodynamic Data of Practical Inorganic Substances*, 2nd ed. Metallurgical Industry Press, Beijing, 2002. ((**in Chinese**))

40. M. Binnewies and E. Milke, *Thermochemical Data of Elements and Compounds*, Wiley-VCH Verlag GmbH, Weinheim/New York, 2002.

41. A.G. Merzhanov, D.Y. Kovalev, V.M. Shkiro and V.I. Ponomarev, Equilibrium of Products of Self-Propagating High-Temperature Synthesis, *Dokl. Phys. Chem.*, 2004, **394**(4-6), p 34-38.

42. A. Nevarez-Rascon, A. Aguilar-Elguezabal and E. Orrantia, Compressive Strength, Hardness and Fracture Toughness of $Al_2O_3$ Whiskers Reinforced ZTA and ATZ Nanocomposites-Weibull Analysis, *Int. J. Refract. Met. Hard Mater.*, 2011, **29**(3), p 333-340.

43. R. Venkataraman, G. Das, S.R. Singh, L.C. Pathak, R.N. Ghosh, B. Venkataraman and R. Krishnamurthy, Study on Influence of Porosity, Pore Size, Spatial and Topological Distribution of Pores on Microhardness of as Plasma Sprayed Ceramic Coatings, *Mater. Sci. Eng. A.*, 2007, **445-446**, p 269-274.

44. B.R. Lawn, Physics of Fracture, *J. Am. Ceram. Soc.*, 1983, **66**, p 83-91.

45. J. Wan, M. Zhou, X.S. Yang, C.Y. Dai, Y. Zhang, W.G. Mao and C. Lu, Fracture Characteristics of Freestanding 8wt%$Y_2O_3$-$ZrO_2$ Coatings by Single Edge Notched Beam and Vickers Indentation Tests, *Mater. Sci. Eng. A.*, 2013, **581**, p 140-144.

46. R. Jaworski, L. Pawlowski, F. Roudet, S. Kozerski and F. Petit, Characterization of Mechanical Properties of Suspension Plasma Sprayed TiO$_2$ Coatings Using Scratch Test, *Surf. Coat. Technol.*, 2008, **202**(12), p 2644-2653.

47. Y. Bautista, J. Gonzalez, J. Gilabert, M.J. Ibanez and V. Sanz, Correlation Between the Wear Resistance, and the Scratch Resistance, for Nanocomposite Coatings, *Prog. Org. Coat.*, 2011, **70**(4), p 178-185.

48. M.S. Kabir, P. Munroe, Z.F. Zhou, and Z.H. Xie, Study of the Structure, Properties, Scratch Resistance and Deformation Behaviour of Graded Cr-CrN-Cr$_{(1-x)}$Al$_x$N coatings, *Ceram. Int.*, 2018, **44**, p 11364-11373.

49. H.T. Chi, L.T. Jiang, G.Q. Chen, P.C. Kang, X. Lin and G.H. Wu, Dry Sliding Friction and Wear Behavior of (TiB$_2$+h-BN)/2024Al Composites, *Mater. Design*, 2015, **87**, p 960-968.

50. Q. Liu, Y.B. Hu, N.J. Chong, Y. Bai, G.Z. Ma, Z.D. Li, M.Y. Bao, H. Zhan, R.J. Wang, Y.W. Sun, Y. Wang and Y.S. Ma, Quantitative Characterization of Carbide Loss and Correlation with Microstructure and Performance of Plasma-Sprayed NiCr-Cr$_3$C$_2$ Metal Carbide Coatings, *J. Therm. Spray Technol.*, 2021, **30**, p 457-470.

51. L. Lin, G.L. Li, H.D. Wang, J.J. Kang, Z.L. Xu and H.J. Wang, Structure and Wear Behavior of NiCr-Cr$_3$C$_2$ Coatings Sprayed by Supersonic Plasma Spraying and High Velocity Oxy-Fuel Technologies, *Appl. Surf. Sci.*, 2015, **356**, p 383-390.

52. D. Davis, M. Srivastava, M. Malathi, B.B. Panigrahi and S. Singh, Effect of Cr$_2$AlC MAX Phase Addition on Strengthening of Ni-Mo-Al Alloy Coating on Piston Ring: Tribological and Twist-Fatigue Life Assessment, *Appl. Surf. Sci.*, 2018, **49**, p 295-303.

53. S. Natarajan, A.E. Edward, K.S. Akhilesh, A. Rajagopal and P.P. Nambiar, Effect of Graphite Addition on the Microstructure, Hardness and Abrasive Wear Behavior of Plasma Sprayed NiCrBSi Coatings, *Mater. Chem. Phys.*, 2016, **175**, p 100-106.

54. F.Y. Zhang, S. Yan, C. Li, Y. Ding, J.N. He, and F.X. Yin, Synthesis and Characterization of MAX phase Cr$_2$AlC Based Composite Coatings by Plasma Spraying and Post Annealing, *J. Eur. Ceram. Soc.*, 2019, **39**, p 5132-5139.

55. S.M. Huang, D.Q. Sun, W.Q. Wang, and H.Y. Xu, Microstructures and Properties of In-Situ TiC Particles Reinforced Ni-Based Composite Coatings Prepared by Plasma Spray Welding, *Ceram. Int.*, 2015, **41**, p 12202-12210.